



Supplementary Materials for

Increased growing-season productivity drives earlier autumn leaf senescence in temperate trees

Deborah Zani, Thomas W. Crowther, Lidong Mo, Susanne S. Renner,
Constantin M. Zohner*

*Corresponding author. Email: constantin.zohner@gmail.com

Published 27 November 2020, *Science* **370**, 1066 (2020)
DOI: 10.1126/science.abd8911

This PDF file includes:

Materials and Methods
Figs. S1 to S9
Tables S1 to S5
References

Other Supplementary Material for this manuscript includes the following:
(available at science.sciencemag.org/content/370/6520/1066/suppl/DC1)

Data Files S1 and S2
MDAR Reproducibility Checklist

Materials and Methods

1. Analysis of Pan European observational data

1.1. *In situ* leaf phenology data set. *In situ* observations of spring leaf-out and autumn leaf senescence dates were collected from the Pan European Phenology Project (www.pep725.eu) (25), which provides open-access phenological data for Europe (mainly Germany, Switzerland, and Austria). Phenology definitions followed the BBCH (Biologische Bundesanstalt, Bundessortenamt und Chemische Industrie) codes (see table S1). For the five deciduous angiosperms, spring leaf-out was defined as the date when the first or 50% of leaf stalks are visible (BBCH11 or BBCH13, respectively), for *Larix decidua* leaf-out was defined as the date when the first leaves separated (mouse ear stage = BBCH10). Leaf senescence was defined as the date when 50% of leaves had lost their green color (BBCH94) or had fallen (BBCH95).

1.2. Data cleaning. Following ref (47), we removed (i) individual time series with less than 15 years of leaf-out and leaf senescence observations, (ii) dates deviating from an individual's median more than 3 times the median absolute deviation, and (iii) time series for which the standard deviation of phenological observations across years was higher than 15 for leaf-out and 20 for leaf senescence. The thresholds differed because the mean absolute deviation for leaf-out time series (8.8) was lower than that for leaf senescence (10.0). After data cleaning, we obtained records of 6 common temperate tree species (5 deciduous angiosperms, 1 deciduous conifer) at 3,855 sites across Central Europe, resulting in a total of 434,226 phenological observations (individuals x year) and 14,626 individual time series (with a median length of 33 years; minimally 15 years, maximally 65 years) during the period 1948–2015. Number of time series per species: *Aesculus hippocastanum*, 3,426; *Betula pendula*, 3,323; *Fagus sylvatica*, 3,037; *Larix decidua*, 1,070; *Quercus robur*, 2,834; *Sorbus aucuparia*, 936.

1.3. Climate and soil data sets. For each site, information on eight climate variables (air temperature, soil temperature in the 0–10 cm layer, precipitation, net short-wave radiation, net long-wave radiation, soil moisture in the 0–10 cm and 10–40 cm layers, and relative humidity) at a spatial resolution of 0.25 arc degrees (approximately 25 km at the equator) and a cadence of 3 hours were derived from the Global Land Data Assimilation System (GLDAS) (48) for the period 1948–2015. We calculated daily means for each of the eight climate variables and the minimum and maximum daily temperatures.

Future projections (2016–2100) of daily mean, minimum and maximum temperatures, precipitation, and net short-wave and long-wave radiation were obtained from a gridded climate data set at 0.5° spatial resolution (approximately 50 km) (49). These projections are based on the RCP 8.5 climate scenario, which assumes continuous emissions throughout the 21st century (business-as-usual scenario).

Means of monthly atmospheric CO₂ concentrations for the Northern Hemisphere were taken from the CMIP6 concentration dataset (29) spanning the period 1948–2015. Future projections of yearly CO₂ emissions (2016–2100) were taken from the Climate Interactive Projections dataset (<https://www.climateinteractive.org>) following the RCP 8.5 climate scenario.

For each site, we extracted physical soil properties (clay and coarse fragment content) from world maps at 250 m spatial resolution through SoilGrids (www.soilgrids.org) (50). Soil texture was computed based on the texture-to-parameter conversion by ref (27), using the Database of Hydraulic Properties of European Soils (HYPRES) implemented in the R package soiltexture (51).

1.4. Seasonal photosynthesis calculation

1.4.1. Summary and validation of seasonal photosynthesis calculation (see detailed model description in sections 1.4.2. and 1.4.3.). Total growing-season net daytime photosynthesis (excluding night-time respiration) was computed on a daily time-step (see table S5 for a description of the abbreviations used in the equations), based on the theory developed in refs (52–54), and following the coupled photosynthesis and stomatal conductance sub-model of LPJ-GUESS (32). We tested our model by comparing its predictions against satellite-data-driven net primary productivity models (55). Because our model parameters were adjusted to predict deciduous tree photosynthesis, for the comparison, we included only deciduous forest pixels with at least 50% forest cover based on the MODIS land cover types and the Hansen forest cover map (56, 57). On average, the R^2 for the predicted versus observed variation in net primary productivity within 291 time series (77 sites), was 0.49, showing that, despite vegetation-type-specific parameters, our model is congruent with remotely-sensed tree vegetation productivity.

To account for the effect of water availability on photosynthesis (30), we included a daily water stress factor, $w(d)$, in our seasonal photosynthesis estimates, which was calculated following the water balance module of LPJ-GUESS (58). The cumulative photosynthesis rate, cA_{tot} , was then obtained by summing the product of the daily net photosynthesis, $A_{tot}(d)$, and the daily water stress factor, $w(d)$, for all days of the growing season. We also computed the cumulative photosynthesis rate not accounting for water stress, cA_{tot-w} , by summing daily total net photosynthesis, $A_{tot}(d)$, for all days of the growing season. Photosynthesis was assumed to start at the date of leaf-out and end at the average date of leaf senescence at the respective site (daylength ~ 11.2 hours). See Fig. S9 for the variation of seasonal photosynthesis in our dataset.

Following ref (28), we additionally developed the cumulative Growing Season Index (cGSI) as a simpler index of seasonal productivity (see section 1.4.3. for details and equations). Leaf productivity for each day of the growing season (leaf-out to leaf senescence) was calculated as the product of temperature, vapor-pressure deficit, and day length. We used vapor pressure deficit to approximate air moisture and CO_2 demand for photosynthetic activity. The R^2 between the Growing Season Index (cGSI) and growing-season net photosynthesis (cA_{tot}) was 0.62, indicating that this simpler representation of growing-season productivity well reflects the variation represented in the parameterized photosynthesis model.

We refer to senescence models based on the coupled photosynthesis and stomatal conductance sub-model of LPJ-GUESS, including or excluding a water-stress factor, as PIA^+ or PIA^- models, the senescence model based on the Growing Season Index is referred to as PIA_{GSI} model (see section 3.3, Figs. 3 and 4, figs. S6–S8 and table S4).

1.4.2. Detailed seasonal photosynthesis calculation. Total growing-season net photosynthesis [$A_{tot}(d)$, $g\ C\ m^{-2}\ day^{-1}$] was based on daily net photosynthesis rates constraint by three limiting states, J_i , J_c and J_e , which correspond to light, Rubisco carboxylation, and electron-transport limited rates, respectively:

$$A_{tot}(d) = \min \left\{ \begin{array}{l} J_i, f_1(APAR, c_1) \\ J_c, f_2(V_{max}, c_2) \\ J_e, f_3(J_i, J_c) \end{array} \right\} - R(d) \quad (1)$$

with $R(d)$ being the rate of daily leaf respiration or CO_2 release [$g\ C\ m^{-2}\ day^{-1}$]. Separate functions were defined for each component (f_{1-3}) and combined for simplification (27). Hence, daily carbon assimilation, $A_{net}(d)$, is given by:

$$A_{net} = APAR * \left(\frac{c_1}{c_2} \right) * [c_2 - (2\theta - 1)s - 2(c_2 - \theta s)\sigma_c] \quad (2)$$

where $APAR$ is the daily integral of absorbed photosynthetically active radiation (PAR, short-wave radiation $J\ m^{-2}\ day^{-1}$) multiplied by the fraction of absorbed photosynthetically active radiation (α_a), which was obtained from the mean growing-season leaf area index (LAI) derived from LPJ-GUESS

(32) [$\alpha_a = 1 - \exp(-0.5 * LAI)$]. For future simulations, we assumed $\alpha_a = 0.5$ since nearly half of the short-wave radiation is intercepted by the canopy (27).

$$APAR = PAR * \alpha_a \quad (3)$$

θ is the shape parameter that determines the degree of collimation by light and Rubisco activity. The coefficients s , c_1 , c_2 , and σ_c are given by:

$$s = \left(\frac{24}{DL}\right) a \quad (4)$$

$$c_1 = \alpha \cdot f_{temp} \cdot \frac{(p_i - \Gamma^*)}{(p_i + 2\Gamma^*)} \quad (5)$$

$$c_2 = \frac{(p_i - \Gamma^*)}{\left(p_i + k_c \left(1 + \frac{p_{O_2}}{k_o}\right)\right)} \quad (6)$$

$$\sigma_s = \left[1 - \frac{(c_2 - s)}{(c_2 - \theta s)}\right]^{0.5} \quad (7)$$

where DL is the daylength [hours]; $a = 0.015$ is a constant for leaf respiration as a fraction of maximum Rubisco capacity (V_{max}) for C_3 plants; $\alpha = 0.08$ is the effective ecosystem-level quantum efficiency of CO_2 uptake in C_3 plants; p_i is the intercellular partial pressure of CO_2 [Pa]:

$$p_i = \lambda p_a \quad (8)$$

where p_a is the atmospheric partial pressure [Pa] and $\lambda = 0.8$ is the optimal ratio of intercellular to ambient CO_2 in C_3 plants. Γ^* is the CO_2 compensation point given by:

$$\Gamma^* = \frac{p_{O_2}}{2\tau} \quad (9)$$

where p_{O_2} is the ambient partial pressure of O_2 [Pa]; $k_o = 3000$ Pa, $k_c = 30$ Pa, $\tau = 2600$ are kinetics parameters with a Q_{10} dependence on temperature.

Finally, f_{temp} defines the temperature response-function to photosynthesis:

$$f_{temp} = low * high \quad (10)$$

$$low = \frac{1}{1 + \exp(k_1 * (k_2 - T))} \quad (11)$$

$$high = 1 - 0.01 \cdot \exp(k_3 * (T - x_3)) \quad (12)$$

$$k_1 = 2 * \log\left(\frac{\frac{1}{0.99} - 1}{x_1 - x_2}\right) \quad (13)$$

$$k_2 = \frac{x_1 + x_2}{2} \quad (14)$$

$$k_3 = \log\left(\frac{\frac{0.99}{0.01}}{x_4 - x_3}\right) \quad (15)$$

where T is the daily mean temperature [$^{\circ}C$], $x_1 = 5$ $^{\circ}C$ and $x_4 = 45$ $^{\circ}C$ correspond to the minimum and maximum temperature limits of photosynthesis, and $x_2 = 18$ $^{\circ}C$ and $x_3 = 25$ $^{\circ}C$ indicate the temperature range optimal for photosynthesis. Following ref (59), these temperature ranges reflect the photosynthesis optima at a latitude of ~ 35 $^{\circ}N$.

The calculation of daily optimal Rubisco capacity [$g\ C\ m^{-2}\ day^{-1}$] followed ref (60):

$$V_{max} = \frac{1}{a} \cdot \frac{c_1}{c_2} \cdot [(2\theta - 1)s - (2\theta s - c_2)\sigma_c] \cdot APAR \cdot c_{mass} \cdot c_q \quad (16)$$

where c_{mass} and c_q are the atomic mass of carbon and the conversion factor for solar radiation at 550 nm from $W\ m^{-2}$ to $mol\ m^{-2}$, respectively.

The light- and Rubisco-limited rates of photosynthesis [$mol\ C\ m^{-2}\ h^{-1}$] and daily leaf respiration [$g\ C\ m^{-2}\ day^{-1}$] were defined as:

$$J_i = \frac{c_1 \cdot APAR \cdot c_{mass} \cdot c_q}{DL} \quad (17)$$

$$J_c = \frac{c_2 \cdot V_{max}}{24} \quad (18)$$

$$R(d) = a \cdot V_{max} \quad (19)$$

Daily net photosynthesis [$A_{net}(d)$, $g\ C\ m^{-2}\ day^{-1}$] was calculated as the difference between gross photosynthesis, $A_{gross}(d)$, and leaf respiration:

$$A_{net}(d) = A_{gross}(d) - R(d) \quad (20)$$

$$A_{gross}(d) = J_i + J_c - \frac{[(J_i + J_c)^2 - 4J_i J_c \theta]^{0.5}}{(2\theta)} DL \quad (21)$$

Finally, total daytime net photosynthesis [g C m⁻² day⁻¹] was obtained from A_{net}(d) by addition of night-time respiration:

$$A_{tot}(d) = A_{net}(d) + \left(1 - \frac{DL}{24}\right) R(d) \quad (22)$$

To account for the effect of water availability on photosynthesis(30), we further included a daily water stress factor, w(d), in our seasonal photosynthesis estimates, which was calculated following the water balance module of LPJ-GUESS (58):

$$w(d) = \min \left\{ 1, \frac{E_{supply}(d)}{E_{demand}(d)} \right\} \quad (23)$$

where the plant-controlled supply function, E_{supply}, is the product of plant root-weighted soil moisture availability, wr, and a plant functional type (PFT)-dependent maximum transpiration rate, i.e. E_{max} = 5 mm d⁻¹ for temperate broad-leaved and boreal needle-leaved summergreen trees.

$$E_{supply}(d) = wr(d) \cdot E_{max} \quad (24)$$

The variable wr gives the ratio between current soil moisture, w(d), and the soil texture-dependent water capacity available for plants (w_{max}).

$$wr(d) = root_1 \left(\frac{w_1(d)}{w_{max}} \right) + root_2 \left(\frac{w_2(d)}{w_{max}} \right) \quad (25)$$

where root₁ and root₂ are the PFT-dependent fractions of roots in the upper (0-10 mm) and lower (10-40 mm) soil layers, respectively.

The atmosphere-controlled demand function, E_{demand}(d), represents the daily unstressed transpiration which occurs when stomatal opening is not limited by reduced water availability in plants. The daily water demand is a hyperbolic function of canopy conductance (61):

$$E_{demand}(d) = \frac{E_{pot}(d)}{1 + \frac{g_{min}}{g_{pot}}} \quad (26)$$

$$E_{pot}(d) = E_q(d) \cdot a_m \quad (27)$$

where E_{pot}(d) is the daily potential evapotranspiration rate determined by multiplying the daily equilibrium rate, E_q(d), with the Priestly-Taylor coefficient, a_m. E_q(d) is calculated from temperature and daylength:

$$E_q(d) = \left(\frac{\Delta}{\Delta + \gamma} \right) \cdot \frac{R_n(d)}{L} \quad (28)$$

$$R_n(d) = R_s(d) - R_l(d) \quad (29)$$

$$R_l(d) = k_e \cdot k_{sb} \cdot T_{soil}^4(d) \quad (30)$$

where the net radiation R_n [W m⁻² d⁻¹] is the downward short-wave radiation minus the upward long-wave flux calculated from soil temperature in kelvin [T_{soil}], the Stefan-Boltzmann constant [W m⁻² K⁻⁴], k_{sb} = 5.670367*10⁻⁸, and an emissivity constant, k_e = 0.9 for deciduous and coniferous plants; γ = 65 Pa K⁻¹ is the psychrometer constant, L = 2.6*10⁶ J kg⁻¹ the latent heat of water vaporization, and Δ the rate of increase of the saturation vapor pressure with daily mean temperature, T(d):

$$\Delta = \frac{2.503 \cdot 10^6 \cdot \exp\left(\frac{17.269 \cdot T(d)}{237.3 + T(d)}\right)}{(237.3 + T(d))^2} \quad (31)$$

g_{min} is the PFT-dependent constant for minimum canopy conductance, and g_{pot} is the non-water stressed canopy conductance [mm d⁻¹] directly related to the photosynthesis rate:

$$g_{pot} = g_{min} + \frac{1.6 \cdot A_{tot}(d)}{c_a(d)(1-\lambda)} \quad (32)$$

$$c_a(d) = \frac{p_a(d)}{press} \quad (33)$$

where A_{tot}(d) is the daily total net photosynthesis [g C m⁻² day⁻¹] calculated as in Equation (22); c_a [ppm] is the daily ambient mole fraction of CO₂ (i.e. the ratio between the atmospheric partial pressure of CO₂, p_a [Pa], and the atmospheric pressure press = 101.325 Pa), and λ = 0.8 is the optimal ratio of intercellular to ambient CO₂ in C₃ plants.

The cumulative photosynthesis rate, cA_{tot} , was then obtained by summing the product of the daily net photosynthesis, $A_{tot}(d)$, and the daily water stress factor, $w(d)$, for all days of the growing season:

$$cA_{tot} = \sum_{d=DoY_{out}}^{d=DL_{d<11}} A_{tot}(d) \cdot w(d) \quad (34)$$

The cumulative photosynthesis rate not accounting for water stress, cA_{tot-w} , was obtained by summing daily total net photosynthesis, $A_{tot}(d)$, for all days of the growing season:

$$cA_{tot-w} = \sum_{d=DoY_{out}}^{d=DL_{d<11}} A_{tot}(d) \quad (35)$$

where the summation starts at the date of leaf flushing, DoY_{out} , and ends at the average date of leaf senescence at the respective site (daylength ~ 11.2 hours) (32). The end date of photosynthesis was fixed to a constant date at each site, independent of inter-annual variations in autumn phenology.

1.4.3. Growing season index

Following ref (28), we additionally developed the cumulative Growing Season Index (cGSI) as a simpler index of seasonal productivity. Leaf productivity for day d , $GSI(d)$ was calculated as the product of temperature (f_{temp}), vapor-pressure deficit ($iVPD$), and daylength (iDL):

$$GSI(d) = iVPD * iDL * f_{temp} \quad (36)$$

Each element of the product is described as a continuous response-function with values ranging between 0 (inactive leaf) and 1 (maximum leaf productivity).

We used vapor pressure deficit ($iVPD$) to approximate air moisture and CO_2 demand for photosynthetic activity, which is a simpler alternative to the stomatal conductance and soil water models as these require detailed information on soil texture, rooting depth, CO_2 concentration, latent heat losses, and precipitation (see section 1.4.2.). We assumed that VPD values below a threshold value ($VPD_{min} = 900$ Pa) do not affect stomatal regulation ($iVPD = 1$) because latent heat losses are minimal (28). Values greater than $VPD_{max} = 4100$ Pa were assumed to cause complete stomatal closure ($iVPD = 0$):

$$iVPD = \begin{cases} 0, & VPD_d \geq VPD_{max} \\ 1 - \frac{VPD_d - VPD_{min}}{VPD_{max} - VPD_{min}}, & VPD_{min} > VPD_d > VPD_{max} \\ 1, & VPD_d \leq VPD_{min} \end{cases} \quad (37)$$

The daily vapor demand, $VPD(d)$, was calculated as the difference between saturation vapor pressure, e_s , and actual vapor pressure, e_a :

$$VPD(d) = e_s - e_a \quad (38)$$

$$e_s = \frac{e^{\circ}(T_{max}) + e^{\circ}(T_{min})}{2} \quad (39)$$

$$e_a = e^{\circ}(T_{dew}) \quad (40)$$

where T_{max} , T_{min} , T_{dew} are maximum, minimum, and dewpoint temperatures, respectively, and e° is the conversion function from $^{\circ}C$ to kPa.

The daylength index, iDL , assumes that photosynthetic capacity peaks when daylength is maximal (62), $DL_{max} = \max\{DL_{GS}\}$, and that no photosynthesis is possible if daylength falls below 11 hours (32), $DL_{min} = 11$:

$$iDL = \begin{cases} 0, & DL_d \leq DL_{min} \\ \frac{DL_d - DL_{min}}{DL_{max} - DL_{min}}, & DL_{max} > DL_d > DL_{min} \\ 1, & DL_d \geq DL_{max} \end{cases} \quad (41)$$

The response-function for optimal temperature, f_{temp} , was calculated as in Equations (10) to (15).

The cumulative Growing Season Index (cGSI) was then calculated as the sum of the daily Growing Season Index, $GSI(d)$, for all days of the growing season following Equations (34) and (35):

$$cGSI = \sum_{d=DoY_{out}}^{d=DL_{d<11}} GSI(d) \quad (42)$$

1.5. Correlation and path analyses. To identify the main drivers of autumn phenology, we tested the importance of seasonal photosynthesis, vapor pressure deficit, and climate and physiological factors that had previously been shown to affect leaf senescence (14, 30, 31) (Fig. S1). We conducted global (i.e., across-site) univariate correlation analyses of leaf senescence dates against: i) observed leaf-out dates, ii) summer temperatures (the average mean temperature of the growing season), iii) autumn temperatures (the average daily minimum temperature of the two months preceding leaf senescence), iv) annual precipitation (number of days with > 2 mm of precipitation across the year), v) summer precipitation (number of days with > 2 mm of precipitation during the driest season), vi) heavy rain days (number of days per year with > 20 mm of precipitation), vii) extreme heat events (number of days with maximum temperature > 35°C during the growing season), viii) annual frosts (number of days with minimum temperature < 0°C per year), ix) frost days in spring (number of frost days during the two months following leaf-out), x) growing-season vapor pressure deficit [VPD_{GS} ; sum of daily $iVPD$ between leaf-out and the date when day length falls below 11 hours; see equation (37)], xi) the cumulative growing-season index (cGSI), and xii) cumulative seasonal photosynthesis rates including and excluding a water deficit index (cA_{tot}/cA_{tot-w}). For each species–site combination, the growing season was defined as the period between leaf-out and senescence, the driest season was defined as the three months with the lowest amount of precipitation (mm/month) during the growing season.

Next, we selected variables with significant correlation coefficients – i.e., seasonal photosynthesis [cA_{tot} , cA_{tot-w} , cGSI; Equations (34), (35), and (42)], leaf-out dates, summer and autumn temperatures, summer precipitation, and VPD_{GS} (Fig. S1) – and applied partial correlation analyses using the R package *ppcor* (63) to characterize the effects of each environmental factor on leaf senescence dates while controlling for the impact of the remaining variables (Figs. 1B and S2). We selected cA_{tot} to represent photosynthesis in the partial correlations, but cA_{tot-w} and cGSI had similar effect sizes.

To explore the causal relationships among the most significant drivers of autumn phenology, we conducted a path analysis using structural equation modelling implemented in the R package *piecewiseSEM* (64). Models were built either i) by accounting only for the direct effect of climatic drivers on autumn phenology (“climate-driven” model), or ii) by including growing-season photosynthesis as a mediator between climatic drivers and autumn phenology (“photosynthesis-driven” model) (Fig. 1c). In both models, site was accounted for as a random effect. To compare model performance, we then conducted a chi-squared difference test and calculated the adjusted R^2 and adjusted root-mean square errors (aRMSEs) (table S2). Site-specific correlation analyses were conducted at the individual time-series level ($N \geq 15$ years), resulting in a total of 14,626 correlation tests. The adjusted R^2 values, the aRMSEs, and the chi-squared difference test showed that the photosynthesis-driven model performed significantly better than the climate-driven model ($R^2 = 0.55$ and 0.13, respectively; Fisher’s C difference = 184.2, $P < 0.001$).

2. Experiments

2.1. Experiment 1. The experiment was conducted in 2017 in the Munich Botanical Garden (48°09’N, 11°30’E; 501 m above sea level) on 5-yr-old individuals of European beech (*Fagus sylvatica*) and Japanese meadowsweet (*Spiraea japonica*). The effects of shading on seasonal photosynthesis and autumn phenology were observed in a total of 28 *Fagus* and 31 *Spiraea* individuals. Plants were obtained from a local nursery and planted on a sunny 10 meters x 10 meters patch outdoors under uniform conditions in a randomized block design. Throughout the experiment, plants were watered, if necessary, to keep soil moisture constant.

The experiment consisted of two treatments plus 2 controls (Fig. 2A). For the *shade* treatment, 1.70 m tall, light-tight Styrofoam plates were placed in front (south) of 5 *Fagus* and 6 *Spiraea* individuals during the growing season from June 1 (shortly after all buds in all individuals had unfolded their leaves) until October 1. The control consisted of 13 individuals per species growing in

full sun. For the *half shade* treatment, the Styrofoam plates were placed in the middle of 5 *Fagus* and 6 *Spiraea* individuals, such that one part of the plant was exposed to sun (control) and the other part was shaded (*half shade* treatment; Fig. S3).

Leaf photosynthesis was monitored three times during summer (July, August, September) on one to two leaves of each individual using photosynthetic light curves (Pulse-amplitude modulated [PAM] chlorophyll fluorometry, Walz, Germany). To obtain the light curves, eight measurements were taken at ambient temperature at 125, 190, 285, 420, 625, 820, 1150, and 1500 $\mu\text{mol photon m}^{-2} \text{s}^{-1}$. We used a customized program that logged at 10-s intervals, starting with equilibration for 2 minutes at 800 $\mu\text{mol photon m}^{-2} \text{s}^{-1}$ and 6 min at 66, which preliminary trials in 2017 suggested was sufficient for leaf equilibration to different light levels. Measurements were taken on a species-rotating basis between 9:00 and 12:00 with replicate individuals of each species done on two to three consecutive days.

To quantify the timing of autumn senescence, we measured seasonal changes in the leaf spectral index (LSI) at 4-week intervals during summer and 2-week intervals during autumn with a SPAD-502 Plus leaf chlorophyll meter (Soil Plant Analysis Development, Minolta Camera Co., Ltd, Tokyo, Japan). Per observational unit (i.e., individual tree for the *shade* treatment or half of an individual tree for the *half shade* treatment), SPAD readings from 10 leaves selected at random were averaged. To calculate the LSI per observational unit, we additionally included the percentage of leaf abscission in autumn, i.e., the already dropped leaves in autumn have an LSI of 0. For example, an individual that lost already 50% of leaves with an LSI of 30 for the remaining leaves has a total LSI of 15 (30×0.5). Per observational unit, we defined leaf senescence onset as the date when the LSI had decreased by 25% relative to the maximum LSI in summer (values between 0% and 100%). We obtained similar results when using the 50% LSI date.

The experimental and observational unit was a single individual for the *shade* treatment and half of an individual for the *half shade* treatment. Given leaf-level photosynthetic properties from the light curve measurements and *in situ* light regime measurements of photosynthetically active radiation (PAR) for each treatment, with an average exposure of 820 $\mu\text{mol photon m}^{-2} \text{s}^{-1}$ for the sun exposed leaves and 190 for the shaded leaves (Fig. S3C), we could calculate the average leaf-level summer photosynthesis per observational unit. We then tested for differences in the timing of autumn senescence and average summer photosynthesis between treatments and controls by performing Welch's t-tests (Fig. 2B,C). The absolute differences in photosynthesis between treatments and controls (Fig. S4) were then converted to relative differences (in %) to simplify comparison with the other experimental results (Fig. 2). Because treatment and control were applied to the same subject (here an individual tree), a paired t-test was performed for the *half shade* treatment. The Shapiro-Wilk-Test was performed to test for significant deviation from the normal distribution of residuals ($P > 0.05$ for all contrasts). The Welch's t-test is not dependent on equal sample sizes. Nevertheless, to ensure that the unequal sample size of the control ($N = 13$) and the *shade* treatment ($N = 5$ and 6 for *Fagus* and *Spiraea*, respectively) did not affect significance estimates, we ran a bootstrap t-test with 999 replicates using the R package MKinfer (v. 0.5).

2.2. Experiment 2. The experiment was conducted in 2019 on 2-yr-old individuals of silver birch (*Betula pendula*) in climate chambers located in Zurich, Switzerland. A total of 40 individuals were used to observe the full-factorial effects of elevated temperatures and CO_2 levels on seasonal photosynthesis and autumn phenology. Plants were obtained from a local nursery and planted in 3 l pots containing a 50/50 sand/peat mixture on 27 March 2019. Before the start of the experiment, all plants were treated with calcium carbonate (MIGROS-Bio carbonated lime), 4.5 g NPK fertilizer (DCM ECO-XTRA 1), and 0.06 g micronutrients (DCM MICRO-MIX). To adjust the slightly acidic soil pH, calcium carbonate was applied in solid form during the potting ($\sim 0.21 \text{ g/l}$ substrate) and two weeks later 300 ml of calcium carbonate dissolved in water (14.1 mg per pot). In August, we treated a suspected fungal infection of some leaves by removing them based on the level of infection,

followed by spraying the plants with a fungicide (Maag ANTI-MALADIES) to prevent further spread.

The experiment consisted of three treatments and an ambient control (Fig. 2A). All treatments were applied from June until winter (until June, all plants were kept at $\sim 4^{\circ}\text{C}$ and 8-h day length). For each month, we ran diurnal cycles resembling average local monthly temperature, humidity, and day length in Zurich, whereby the temperatures of the control were kept $\sim 2^{\circ}\text{C}$ below average. To account for the late start of the experiment, we shifted the monthly climate conditions by two months (e.g., the climate settings for July reflected those typically occurring in May). The monthly minima and maxima of daily temperatures, humidity and day length are shown in table S6. CO_2 levels of the control were set to 400 ppm. In the *high CO₂* treatment, plants were exposed to 800 ppm [CO_2], in the *high temperature* treatment, chambers were kept 5°C warmer than the control, while in the *high temperature + high CO₂* treatment, plants were kept at 800 ppm [CO_2] and $+5^{\circ}\text{C}$ above control temperatures. Throughout the experiment, plants were watered regularly to keep soil moisture constant. Every month, treatments were rotated between chambers to avoid “chamber effects”.

Leaf net photosynthesis (CO_2 uptake per leaf area) was monitored monthly during spring and summer on one leaf of each of the 40 individuals using a portable infrared gas analyzer (LI-6800, Li-Cor, Lincoln, NE) with a 3x3cm leaf chamber. Leaf chamber temperatures during the measurements reflected the daily temperatures at noon in each chamber. Humidity was set to 68%, leaf chamber CO_2 to 400ppm (low CO_2 treatments) and 800ppm (high CO_2 treatments), and leaf chamber light intensity to $250\ \mu\text{mol m}^{-2}\text{s}^{-2}$ (90% red, 10% blue). Measurements were taken between 2 to 6 hours after sunrise with replicate individuals of each treatment done on four consecutive days. Because leaves were not yet full-sized and did not fully cover the leaf chamber of our portable infrared gas analyzer in the first measurements, we corrected photosynthesis values for leaf size differences using leaf size measurements from scaled photographs. Spring-to-summer photosynthesis was then calculated for each individual as the sum of daily photosynthesis from leaf-out in June until mid-September. To account for daylength, we calculated daily photosynthesis values by multiplying hourly photosynthesis values with the number of full light hours.

The timing of autumn senescence was quantified in four individuals per treatment as described in experiment 1. Per individual, the mean of SPAD readings from nine average leaves was calculated.

To test for differences in the timing of autumn senescence and spring-to-summer photosynthesis between treatments and the control we performed a post-hoc Tukey-Kramer test (Figs. 2B,C and S5). As in experiment 1, the absolute differences in photosynthesis between treatments and controls (Fig. S5A) were then converted to relative differences (in %) (Fig. 2B). The experimental and observational unit was a single individual. The Shapiro-Wilk-Test was performed to test for normal distribution of residuals ($P > 0.05$).

To test for a direct correlation between photosynthesis and leaf senescence, we additionally ran a multiple linear regression model, including leaf-level spring-to-summer photosynthesis and the number of leaves per individual before the onset of leaf senescence in October as predictor variables and senescence date as dependent variable. The number of leaves per individual was included to account for the possibility that treatment-level differences in the absolute amount of leaves per tree (indicating differences in sink strength) could have affected senescence dates. The results showed that leaf-level photosynthesis had a large negative effect on senescence dates (~ 5 days advance per each 10% increase in photosynthesis; standardized regression coefficient = -0.65, $P = 0.009$), while the number of leaves per individual had no effect on senescence dates (standardized regression coefficient = -0.01, $P = 0.95$) and did not differ among treatments (ANOVA P -value = 0.70).

3. Autumn phenology modelling

We developed a new autumn phenology model including a parameter for seasonal photosynthesis (hereafter referred to as *PIA* – Photosynthesis-Influenced Autumn phenology – model) and tested its performance and predictions against seven common process-based phenology models using the *in situ* observations of spring leaf-out and autumn leaf senescence dates from the Pan European

Phenology Project (see section 1.1.). Previous models are based on cold temperature (cold-degree-day) accumulation and daylength (*first-generation models*) and can include information on growing-season factors, such as spring leaf-out timing, growing-season temperature, and drought events (*second-generation models*).

3.1. First generation models. In the most basic autumn phenology model, autumn senescence is modelled as a function of low temperature accumulation (CDD = Cold-Degree-Day model) (65). The starting date of the CDD model (D_{start}) is defined as the first day when daily minimum temperature, $T_{min,d}$, is lower than a temperature threshold, T_{start} , after the 200th day of the year:

$$D_{start} = \min_d \{T_{min,d} < 200 < T_{start}\} \quad (43)$$

Variations of this model include daylength (DM (12) = Delpierre model and TPM (66) = Low Temperature And Photoperiod Multiplicative model), and the cold-degree-day summation starts when daylength, DL_d , is lower than a threshold, DL_{start} , after the summer solstice (DoY = 173):

$$D_{start} = \min_d \{DL_d < 173 < DL_{start}\} \quad (44)$$

In the CDD model, the daily rate of leaf senescence, $R_{LS,CDD}(d)$ is a function of cold-degree-day accumulation below a certain temperature threshold, T_{start} :

$$R_{LS,CDD}(d) = T_{min,d} - T_{start} \quad (45)$$

In the DM model (12), modifiers are added to include the effect of daylength. Leaf senescence rates can either monotonically decrease (DM1 model) or increase (DM2 model) with daylength, DL_d [Equations (46) and (47), respectively]:

$$R_{LS,DM1}(d) = (T_{min,d} - T_{start}) * \frac{DL_d}{DL_{start}} \quad (46)$$

$$R_{LS,DM2}(d) = (T_{min,d} - T_{start}) * \left(1 - \frac{DL_d}{DL_{start}}\right) \quad (47)$$

Leaf senescence rates in the TPM (66) model are modelled as an exponential function of the arithmetic product between daylength and minimum temperature:

$$R_{LS,TPM}(d) = \frac{1}{1 + \exp(a * (T_{min,d} * DL_d - b))} \quad (48)$$

where a and b are free parameters and $T_{min,d}$ is the minimum temperature and DL_d is the daylength on day d .

3.2. Second generation models. These models are further modifications of the DM model and account for growing-season components, such as spring leaf-out ($SIAM$ = Spring Influenced Autumn Model) (15), growing-season mean temperature (TDM = Leafy Season Temperature Delpierre model), and leafy season precipitation ($TPDM$ = Temperature- and precipitation-influenced Delpierre model) (11).

In first- and second-generation models, the leaf senescence state, S_{LS} , is the sum of daily leaf senescence rates from D_{start} until a critical value, Y_{crit} , is reached, which corresponds to the occurrence of leaf senescence at a specific date, DoY_{LS} :

$$S_{LS} = \sum_{d=D_{start}}^{DoY_{LS}} R_{LS}(d) = Y_{crit} \quad (49)$$

In *first-generation* models, the critical value, Y_{crit} , is a free parameter optimized across the modelling unit, e.g., at the time-series level. In second-generation models, Y_{crit} is a linear function of spring leaf-out (15), growing-season temperature (11), or a combination of growing-season temperature and precipitation (11):

$$Y_{crit,SIAM} = c + d * S_a \quad (50)$$

$$Y_{crit,TDM} = e + f * temp_{summer} \quad (51)$$

$$Y_{crit,TPDM} = g + h * temp_{summer} + i * RD_{summer} \quad (52)$$

where c to i are free parameters governing the effect of changes in the respective factor on autumn senescence, S_a [Equation (50)] is the observed spring anomaly (deviation from the mean observed leaf-out date at each site) (15), $temp_{summer}$ [Equations (51) and (52)] is the growing-season mean

temperature (11), and RD_{summer} [Equation (52)] is the low precipitation index (number of days with > 2 mm of precipitation during the driest season) (11).

3.3. PIA (Photosynthesis-Influenced Autumn phenology) model. Building on the above-mentioned existing models, we developed a model that includes information on seasonal photosynthesis (the cumulative total daytime net photosynthesis, cA_{tot} [PIA^+ model], the cumulative total daytime net photosynthesis not accounting for water stress, $cA_{\text{tot-w}}$ [PIA^- model], or the cumulative Growing Season Index, $cGSI$ [PIA_{GSI} model]). These models modify the critical cold-degree-day threshold (Y_{crit}) in dependence of seasonal photosynthesis. Motivated by the linear relationship between seasonal photosynthesis and autumn senescence dates (Fig. 1A), Y_{crit} was modelled as a linear function of the annual productivity anomaly:

$$Y_{\text{crit}} = j + k * cA_{\text{tot}} \quad (53)$$

$$Y_{\text{crit}} = l + m * cA_{\text{tot-w}} \quad (54)$$

$$Y_{\text{crit}} = n + o * cGSI \quad (55)$$

where j to o are free parameters governing the effect of changes in the respective factor on autumn senescence, and cA_{tot} , $cA_{\text{tot-w}}$, and $cGSI$ [Equations (53) to (55)] are the modelled productivity anomalies, i.e., the difference between photosynthesis in a given year and the site-level mean photosynthesis.

For the *second-generation* models (SIAM (15), TDM (11), TPDM (11)) and our new *PIA* model (PIA^+ , PIA^- , PIA_{GSI}), we evaluated the performance of the four existing leaf senescence rate functions [Equations (45) to (48)] based on the root-mean-square errors (RMSEs) across time series. Equation (48) was chosen for all models and time series because it resulted in the lowest RMSE in >90% of cases.

3.4. Model calibration. Model parametrization was conducted using the R-package PHENOR (67). Model parameters were optimized using the GenSA algorithm, which combines both the Boltzmann machine and faster Cauchy machine simulated annealing approaches for fast optimizations (68). Following ref (67), the number of iterations was set to 40,000. Models were calibrated at the individual time-series scale, assuming that the critical cold-degree-day sum, Y_{crit} , varies among sites and species (30).

3.5. Model performance. We evaluated the quality of the model predictions with three performance indexes of observed (y-axis) vs. predicted (x-axis) autumn senescence dates: 1) the overall fit (R^2 values); 2) the error fit (root mean square error, RMSE); and 3) the accuracy of the fit (slope values). Additionally, the site-specific performance of the models was evaluated using 5-fold cross-validation over the observation period at the time-series scale (“site-specific validation”) (69), allowing us to test whether projected leaf senescence dates capture observed temporal trends.

3.6. Future projections. To evaluate the implications of our new findings for future autumn phenology and growing-season projections, we forecasted the timing of autumn senescence until 2100 based on the two best-performing models per model category (*first-generation*: CDD and TPM; *second-generation*: SIAM and TPDM; *PIA*: PIA_{GSI} and PIA^+). Future projections of daily mean, minimum and maximum temperatures, precipitation, and net short-wave and long-wave radiation followed the RCP 8.5 climate scenario (49) (section 1.3.). Future projections of leaf-out dates were obtained using three of the best performing spring phenology models from the literature [AT (70), M1 (71) and PM1 (71, 72)]. These models give very similar leaf-out predictions (see Fig. 4 in ref (7)) and leaf-out model choice therefore did not affect our leaf senescence projections. For the final analysis, we used future leaf-out predictions of the M1 model.

Figures S1 to S9

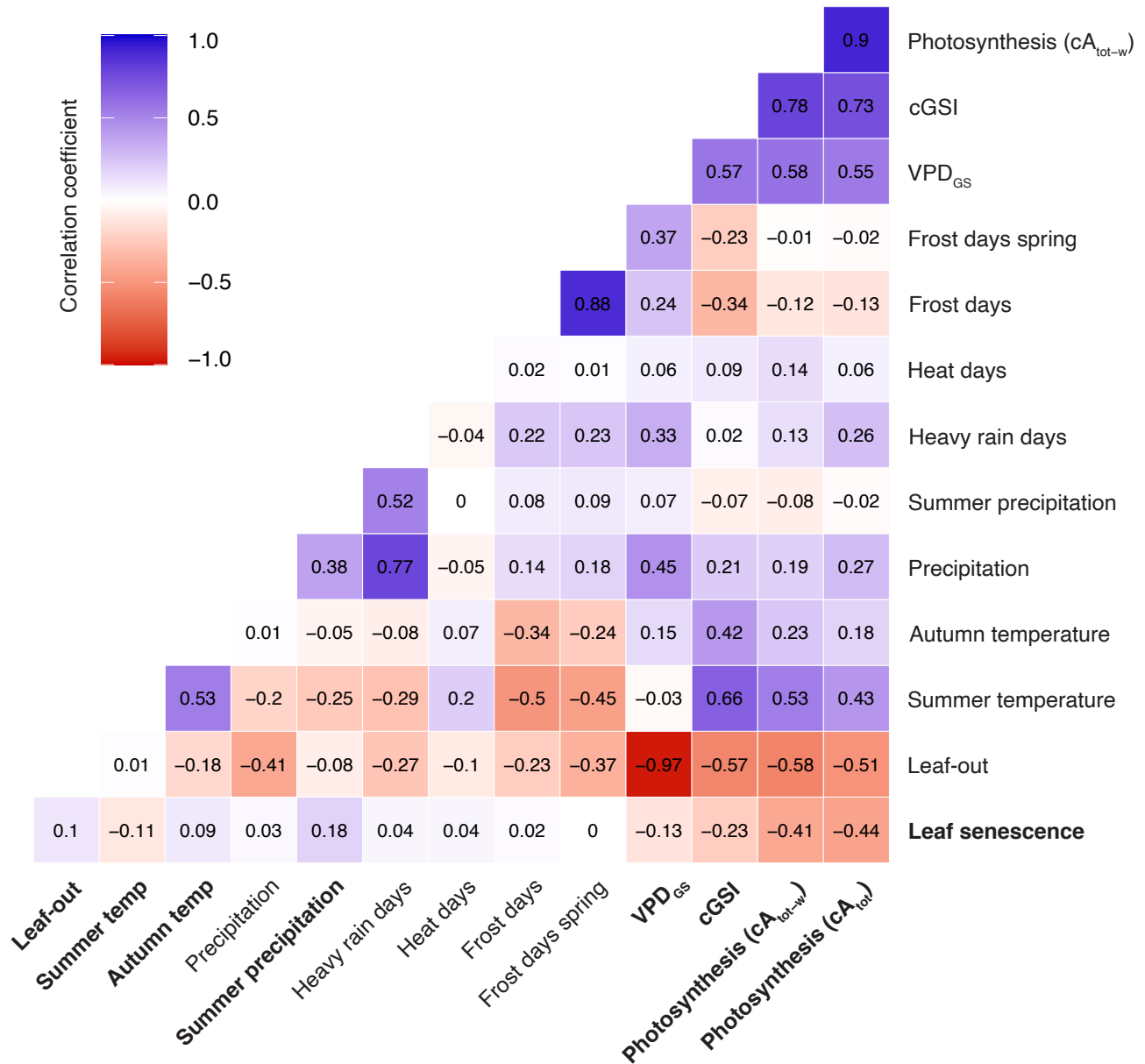


Fig. S1. The environmental and intrinsic drivers of autumn phenology. Univariate Pearson's correlation coefficients for the effects of 13 variables on autumn leaf senescence dates across all 434,226 observations: leaf-out date, summer temperature (average temperature during the growing season), autumn temperature (average minimum temperature during autumn, i.e., 2 months before leaf senescence), precipitation (rainy days per year, i.e., the number of days with > 2 mm of precipitation), summer precipitation (rainy days during the three months of the growing season with the lowest amount of precipitation), heavy rain days (number of days per year with > 20 mm of precipitation), extreme heat events (number of days with maximum temperature > 35°C; Heat days), frost days (number of days with minimum temperature < 0°C), frost days in spring (number of frost days during the 2 months after leaf-out), growing-season vapor pressure deficit (VPD_{GS}), Materials and Methods Equation (37)], the cumulative growing season index (cGSI), and cumulative seasonal photosynthesis rate including and excluding a water deficit index (cA_{tot} / cA_{tot-w}). Variables that showed a significant ($P < 0.05$) effect on senescence dates are highlighted in bold.

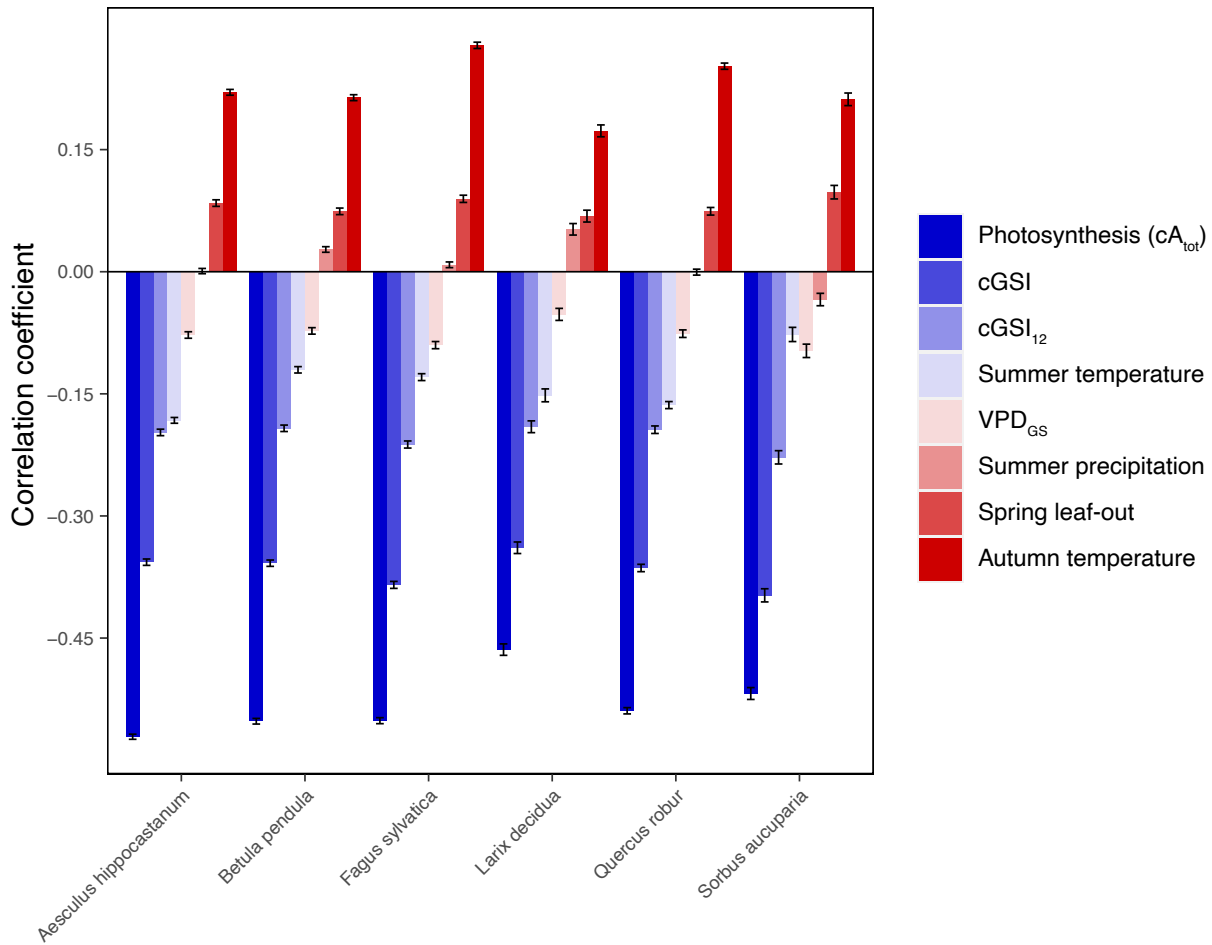
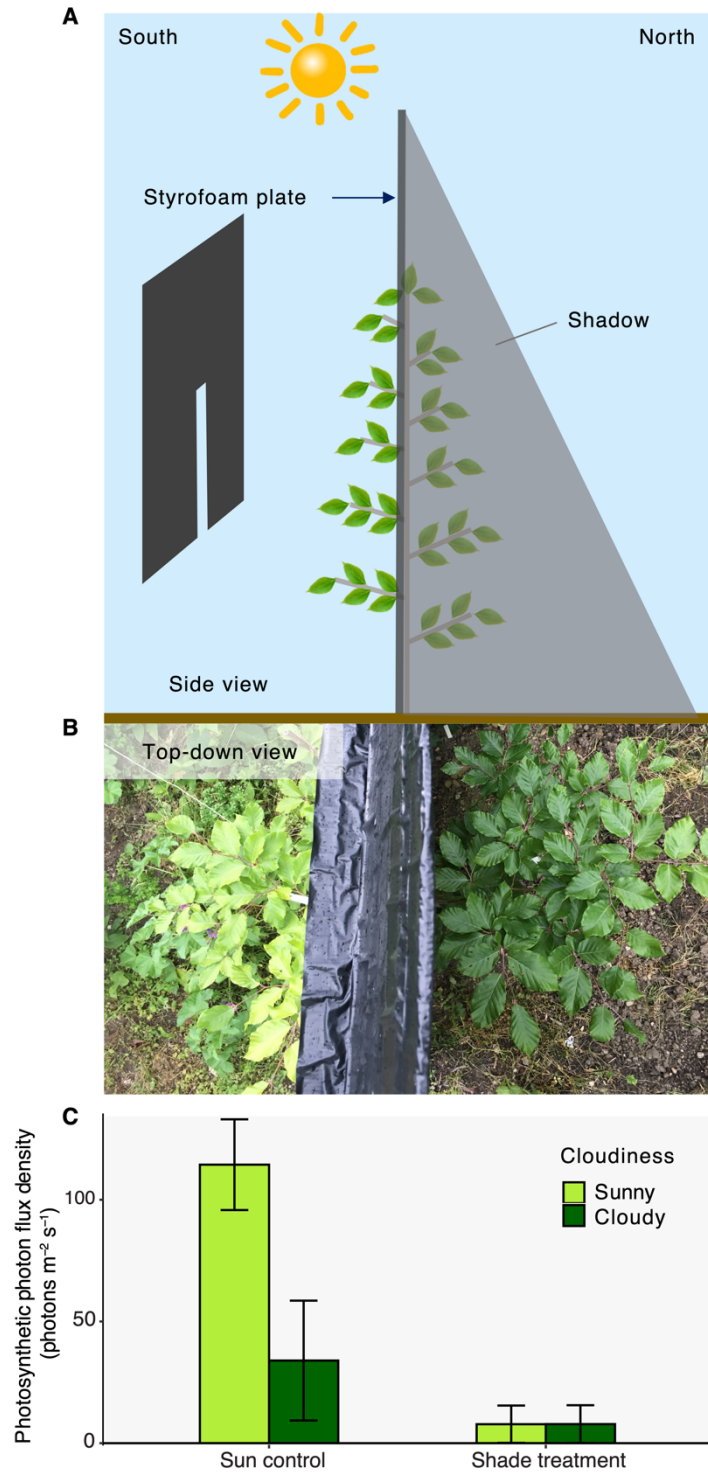


Fig. S2. The effects of seasonal photosynthesis, spring phenology, and relevant climate variables on autumn senescence dates for six Central European species. Bars show mean standardized correlation coefficients (± 2 standard errors). *Photosynthesis* (cA_{tot}) = cumulative net photosynthetic rate during the growing season, including a water deficit index; *cGSI* = cumulative growing-season index, with growing season defined as the period between leaf-out and leaf senescence; *cGSI₁₂* = cumulative growing-season index, with growing season defined as the period between leaf-out and the September equinox (day length = 12 hours). *Summer temperature* = average temperature during the growing season; *Growing-season vapor pressure deficit* (VPD_{GS}) = sum of iVPD for each day of the growing season [equation (37)]; *Summer precipitation* = number of rainy days (> 2 mm of precipitation) during the driest season (i.e. the three months with the lowest amount of precipitation during the growing season); *Spring leaf-out* = observed leaf-out date; *Autumn temperature* = average daily minimum temperature during autumn (i.e., 2 months before the average leaf senescence date per species and site). Number of analyzed time series per species: *Aesculus hippocastanum*, 3,426; *Betula pendula*, 3,323; *Fagus sylvatica*, 3,037; *Larix decidua*, 1,070; *Quercus robur*, 2,834; *Sorbus aucuparia*, 936.

Fig. S3. Setup of experiment 1 (shade experiment). (A) For the *half shade* treatment, Styrofoam plates with a slot in which the tree stem fit were placed in the middle of trees in west–east direction, so that tree branches were either facing south (being exposed to full sun = control) or north (being exposed to shade = *half shade* treatment). For the *shade* treatment, Styrofoam plates without slot were placed in front (south) of the tree and compared to sun-exposed plants (shown in Fig. 2A). (B) Top-down photograph of a *Fagus sylvatica* tree, showing the sunny (left) and shaded (right) halves of the plant. (C) Comparison of light regimes south and north of the Styrofoam plates. At each side, photosynthetic photon flux densities (PPFDs) were measured 18 times during the 2017 growing season. Bars show mean PPFDs \pm 2 standard deviations for the sun-exposed and shaded parts. PPFD values are shown for sunny and cloudy days (light green and dark green bars, respectively).



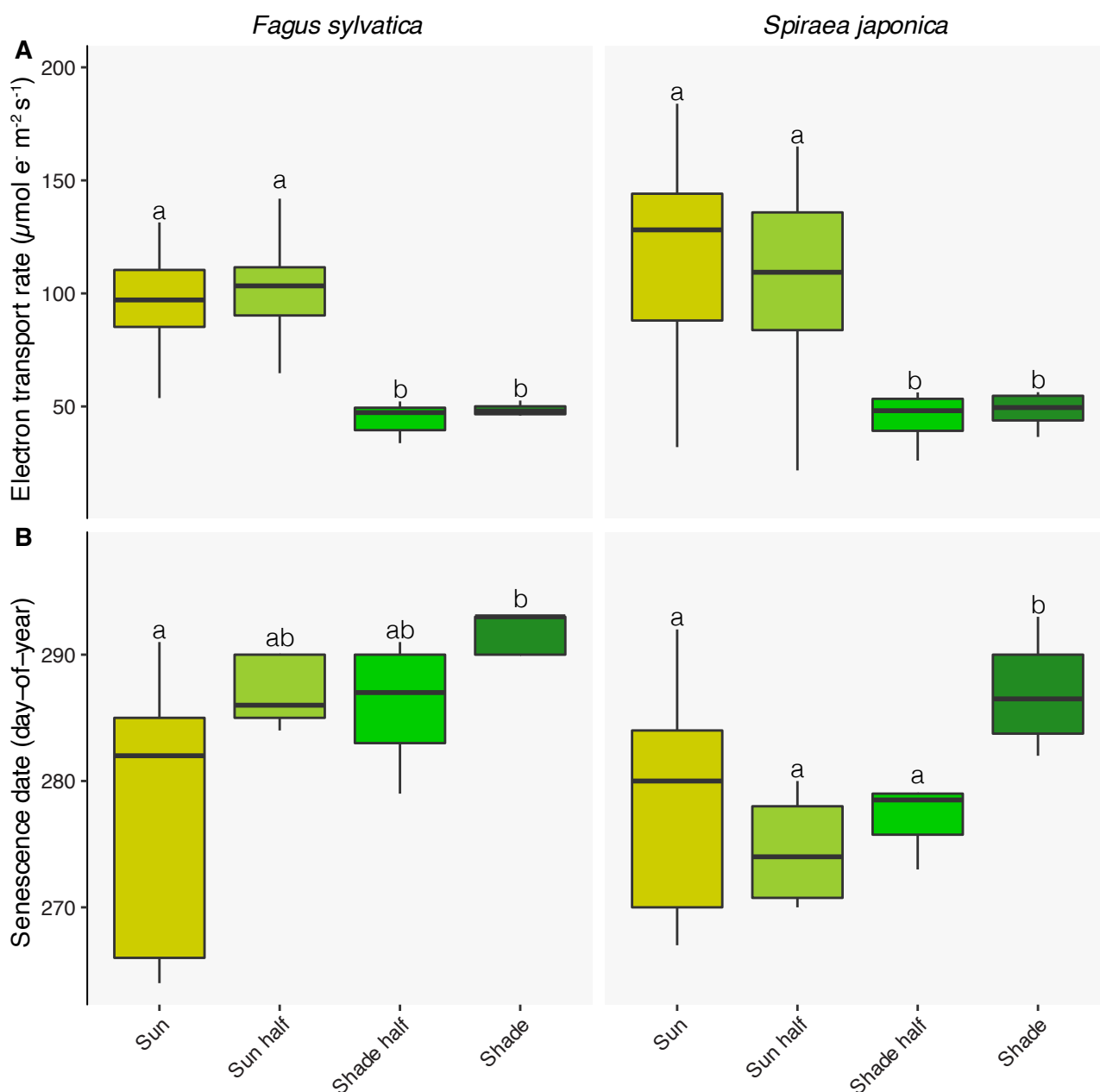


Fig. S4. Detailed results of experiment 1. (A) Mean leaf-level summer photosynthetic activity of *Fagus sylvatica* and *Spiraea japonica* for the four treatments (sun-exposed, half of plant exposed to sun, half of plant exposed to shade, shaded). Values are mean electron transport rates for each treatment. (B) Senescence dates (in day-of-year) for each treatment. Senescence dates were defined as the date when the leaf chlorophyll content dropped by 25% relative to the maximum (see Materials and Methods). Letters above boxplots indicate which treatments differ from each other (Kruskal-Wallis multiple comparisons (A) or Tukey-Kramer test (B), $P < 0.05$).

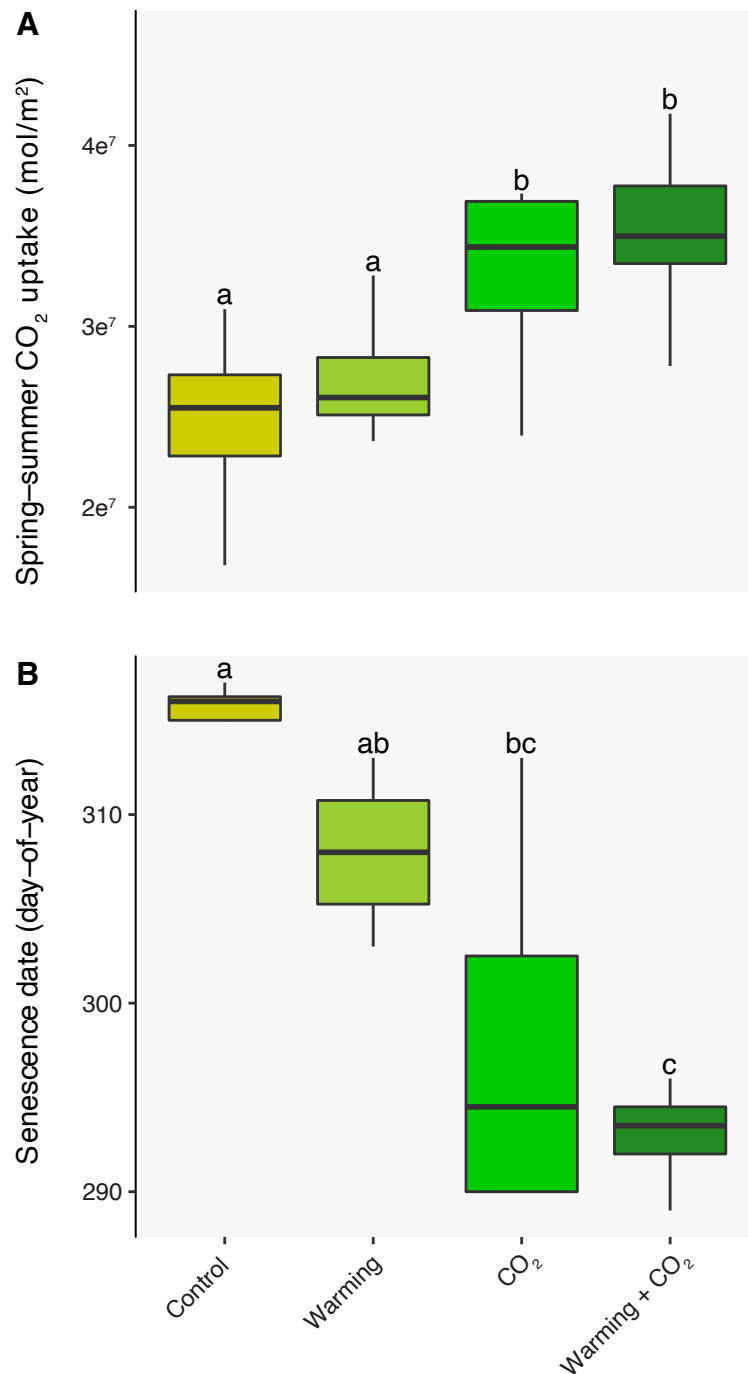


Fig. S5. Detailed results of experiment 2. (A) Spring-summer photosynthetic activity of *Betula pendula* for the four controlled treatments (ambient control, +5°C warming, high CO₂ [800 ppm], warming and high CO₂). Values represent the cumulative leaf-level CO₂ uptake from leaf-out in June until mid-September in mol/m². (B) Senescence dates (in day-of-year) for each treatment. Senescence dates were defined as the date when the leaf chlorophyll content dropped by 25% relative to the maximum (see Materials and Methods). Letters above boxplots indicate which treatments differ from each other (Tukey-Kramer test, $P < 0.05$).

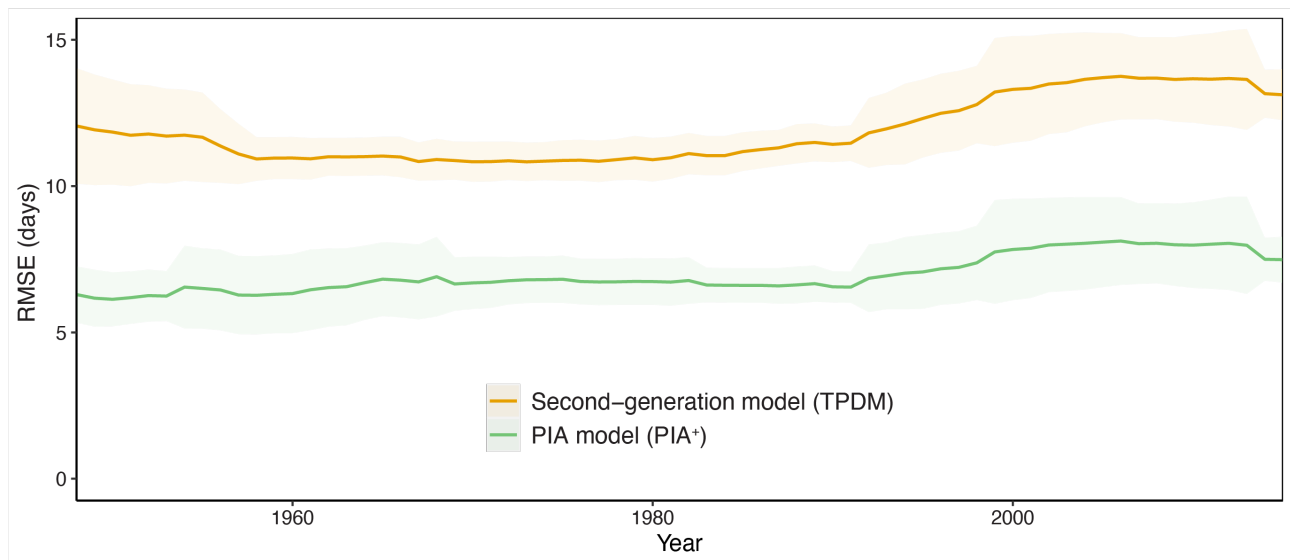


Fig. S6. Model performance across time. Root-mean-square errors (RMSEs) of observed versus predicted senescence dates within each year for the best-performing 2nd generation model (TPDM) and the PIA⁺ model. Plot shows 15-year moving averages of RMSEs (mean \pm SD).

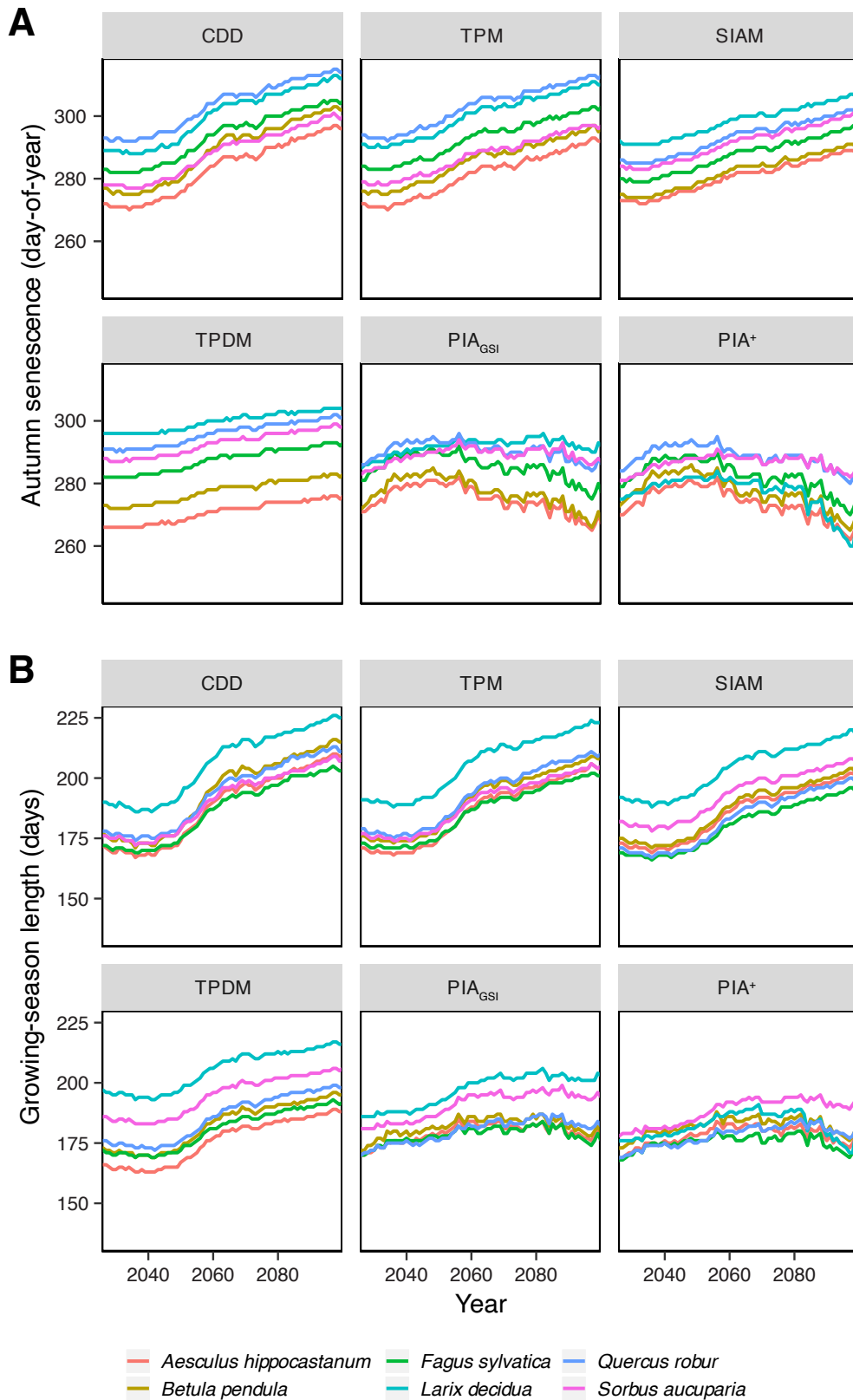


Fig. S7. Future projections of autumn senescence dates (A) and growing-season length (B) for six Central European species. Projections (15-year moving averages) are based on *first-generation* (CDD and TPM), *second-generation* (SIAM and TPDM), and the *PIA* (PIA^+ and PIA_{GSI}) models, and follow the RCP 8.5 climate scenario. Future projections of spring leaf-out dates came from the M1 model (7, 71). Number of analyzed time series per species: *Aesculus hippocastanum*, 3,305; *Betula pendula*, 3,225; *Fagus sylvatica*, 2,900; *Larix decidua*, 1,065; *Quercus robur*, 2,819; *Sorbus aucuparia*, 931.

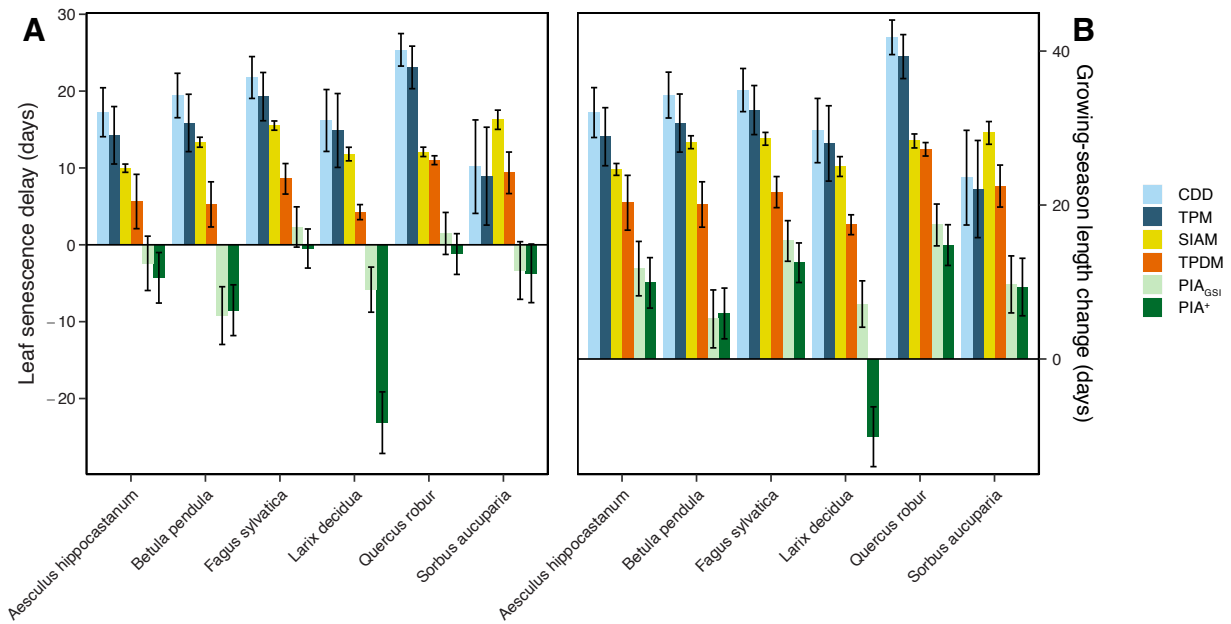


Fig. S8. Future delays in autumn senescence dates (A) and increases in growing-season length (B) for six Central European species. (A) Estimated delays in leaf senescence by the end of the 21st century (2080–2100) compared to the average senescence dates observed between 1990–2010. (B) Estimated increases in growing-season length by the end of the 21st century (2080–2100) compared to the average growing-season length observed between 1990–2010 based on the RCP8.5 climate scenario. Future autumn senescence date predictions are based on *first-generation* (CDD and TPM), *second-generation* (SIAM and TPDM), and the *PIA* (PIA_{GSI} and PIA⁺) models; future leaf-out date predictions are based on the M1 model. For the number of analyzed time series per species see Fig. S7.

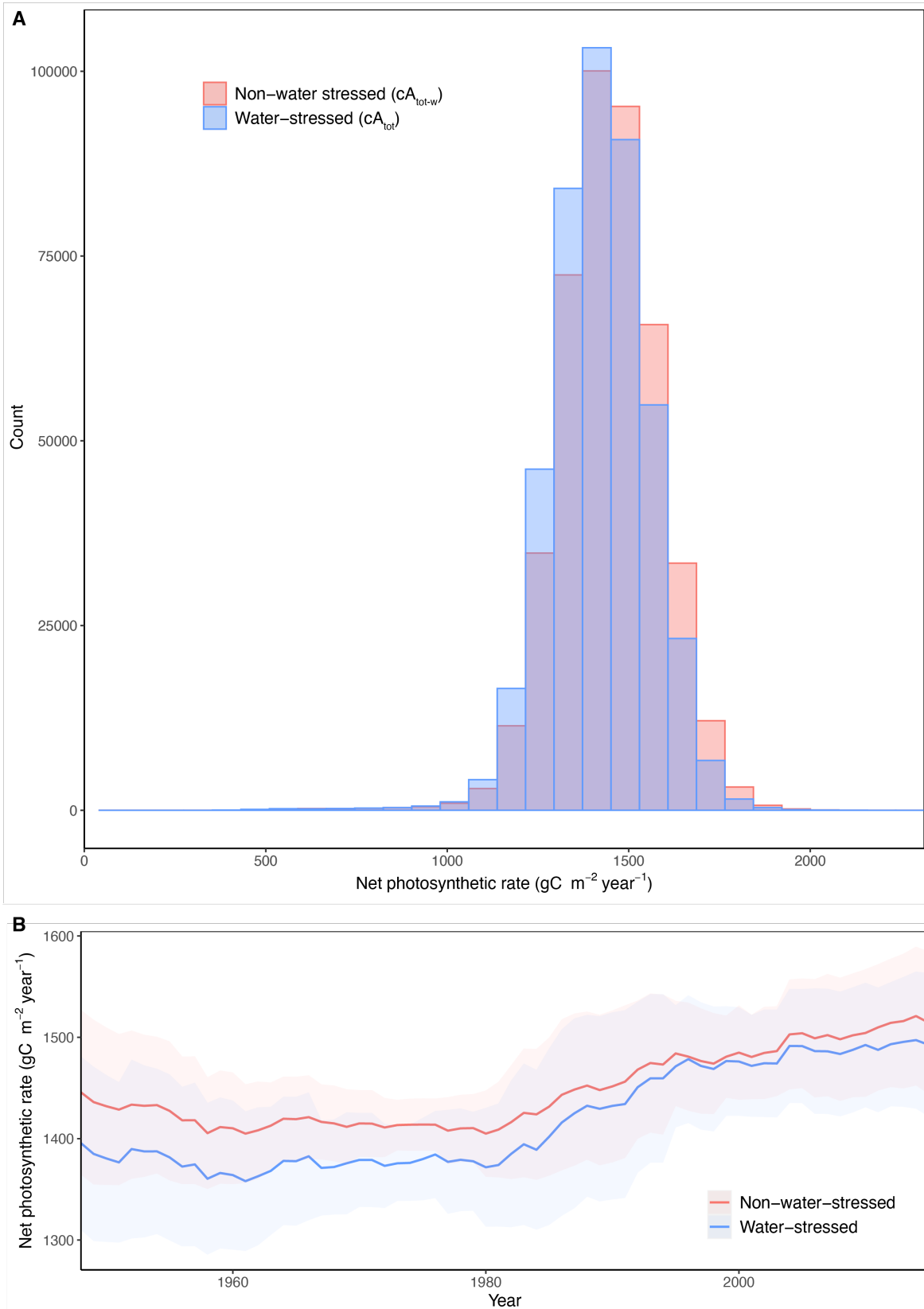


Fig. S9. Variation in annual net photosynthesis in our dataset. Net daytime photosynthesis was estimated from a parameterized photosynthesis model (27). **(A)** Frequency distribution showing the total variation across years and sites. **(B)** Temporal variation in annual photosynthesis. Blue: Model including a water stress factor; red: model not accounting for water stress.

Tables S1 to S5

Table S1. Properties of the phenological data used in this study. Sites = number of sites per species with at least 15 years of leaf-out and leaf senescence observations; Observations = total number of observations per species across years and sites; Leaf-out / Leaf senescence date = mean \pm SD day-of-year of leaf-out (defined as BBCH10 for *Larix decidua* and BBCH11/13 for the other species) and leaf senescence (defined as BBCH94/95).

Species	Sites	Observations	Leaf-out date	Leaf senescence date
<i>Aesculus hippocastanum</i>	3,426	108,669	112 \pm 12	277 \pm 12
<i>Betula pendula</i>	3,323	103,858	111 \pm 11	279 \pm 13
<i>Fagus sylvatica</i>	3,037	93,441	119 \pm 10	282 \pm 12
<i>Larix decidua</i>	1,070	22,588	101 \pm 11	294 \pm 13
<i>Quercus robur</i>	2,834	86,993	125 \pm 11	288 \pm 12
<i>Sorbus aucuparia</i>	936	18,697	107 \pm 10	288 \pm 14

BBCH10: First leaves separated (mouse ear)

BBCH11: Leaf unfolding (first visible leaf stalk)

BBCH13: Leaf unfolding (50%)

BBCH94: Autumnal colouring of leaves (50%)

BBCH95: Autumnal fall of leaves (50%)

Table S2. Details of the structural equation models (SEMs) excluding (“Climate-driven model”, Fig. 1C left-panel) or including (“Photosynthesis-driven model”, Fig. 1C right-panel) net daytime photosynthesis as a predictor of leaf senescence. To compare model performance, we calculated the adjusted coefficient of determination (R^2), the adjusted root-mean square error (aRMSE), as well as the chi-squared difference test based on Fisher’s C statistic. * $P < 0.05$, ** $P < 0.01$, *** $P < 0.001$.

Model	Overall fit	Response	Predictor	Standardized direct effect
Climate	$R^2 = 0.13$ aRMSE = 0.20 Fisher’s C = 276.31	Autumn anomaly	Spring anomaly	0.05***
		Autumn anomaly	Autumn temperature	0.35***
		Autumn anomaly	Summer temperature	-0.39***
		Autumn anomaly	Precipitation	-0.07***
		Autumn anomaly	VPD _{GS}	-0.11***
Full	$R^2 = 0.55$ aRMSE = 0.17 Fisher’s C = 460.52***	Autumn anomaly	Photosynthesis	-0.61***
		Autumn anomaly	Autumn temperature	0.24***
		Photosynthesis	Spring anomaly	-0.14***
		Photosynthesis	Vapour pressure deficit	0.39***
		Photosynthesis	Summer temperature	0.54***
		Photosynthesis	VPD _{GS}	0.16***

Table S3. Process-based models of autumn phenology. Models are grouped by implemented processes and drivers: autumn cold-degree-days (CDD_{aut}), autumn daylength (DL_{aut}), spring leaf-out date (DoY_{out}), spring leaf-out anomaly (S_a), water stress (W_s), growing-season temperature (T_{GS}), daylength (DL_{GS}), vapor pressure deficit (VPD_{GS}), precipitation (Pr_{GS}), net radiation (Rad_{GS}), CO_2 concentration (C_{GS}). No. of free parameters refers to the number of parameters defined by the training data.

Model types	Drivers	No. of free parameters	References
<i>First-generation models</i>			
Cold-degree-day model (CDD)	CDD_{aut}	2	(28)
Delpierre model 1 (DM1)	CDD_{aut} , DL_{aut}	3	(12)
Delpierre model 2 (DM2)	CDD_{aut} , DL_{aut}	3	(12)
Low temperature and photoperiod multiplicative model (TPM)	CDD_{aut} , DL_{aut}	4	(66)
<i>Second-generation models</i>			
Spring-influenced autumn model (SIAM)	CDD_{aut} , DL_{aut} , S_a	+2	(15)
Temperature-influenced DM (TDM)	CDD_{aut} , DL_{aut} , T_{GS}	+2	(11)
Temperature- and Precipitation-influenced DM (TPDM)	CDD_{aut} , DL_{aut} , T_{GS} , W_s	+3	(11)
<i>PIA (Photosynthesis-Influenced Autumn phenology) models</i>			
Growing-season index model (PIA_{GSI})	CDD_{aut} , DL_{aut} , DoY_{out} , T_{GS} , DL_{GS} , VPD_{GS}	+2	
Non-water-stressed model (PIA^-)	CDD_{aut} , DL_{aut} , DoY_{out} , T_{GS} , DL_{GS} , Pr_{GS} , Rad_{GS} , C_{GS}	+2	
Water-stressed model (PIA^+)	CDD_{aut} , DL_{aut} , DoY_{out} , T_{GS} , DL_{GS} , Pr_{GS} , Rad_{GS} , C_{GS} , W_s	+2	

Table S4. Site-specific performance and validation of the 10 process-based autumn phenology models. Statistic performance and validation (mean \pm SD) of observed *vs.* predicted values of autumn anomaly across all species and for each of the 6 study species: Model = model name; N = number of analysed time series; R^2 = overall model fit (coefficients of determination); RMSE = root mean square errors of model predictions; Slope = slope of observed *vs.* predicted values to characterize the accuracy of the model fit; $RMSE_{xval}$ = site-specific validation using 5-fold cross-validation.

Species	Model	N	R^2	RMSE	Slope	$RMSE_{xval}$
All species	CDD	14,626	0.10 \pm 0.11	9.54 \pm 2.79	0.48 \pm 0.72	10.22 \pm 1.02
	DM1		0.16 \pm 0.12	9.02 \pm 2.70	1.97 \pm 2.33	9.53 \pm 1.05
	DM2		0.13 \pm 0.11	9.22 \pm 2.71	1.96 \pm 2.09	9.93 \pm 1.06
	TPM		0.21 \pm 0.13	8.79 \pm 2.70	1.93 \pm 1.82	9.46 \pm 1.07
	SIAM		0.58 \pm 0.19	10.67 \pm 5.52	0.70 \pm 1.67	9.86 \pm 3.35
	TDM		0.62 \pm 0.18	11.01 \pm 5.66	0.74 \pm 0.16	10.26 \pm 3.35
	TPDM		0.62 \pm 0.18	10.87 \pm 5.48	0.74 \pm 1.16	10.16 \pm 3.35
	PIA _{GSI}		0.78 \pm 0.14	7.30 \pm 4.04	0.94 \pm 0.08	6.72 \pm 1.03
	PIA ⁻		0.78 \pm 0.14	6.99 \pm 3.84	0.94 \pm 0.08	6.39 \pm 0.93
	PIA ⁺		0.78 \pm 0.14	6.41 \pm 3.67	0.94 \pm 0.08	6.17 \pm 0.74
<i>Aesculus hippocastanum</i>	CDD	3,426	0.09 \pm 0.10	9.45 \pm 2.54	0.43 \pm 0.73	10.21 \pm 1.03
	DM1		0.15 \pm 0.11	8.93 \pm 2.44	2.25 \pm 2.48	9.55 \pm 1.04
	DM2		0.12 \pm 0.10	9.10 \pm 2.44	2.08 \pm 2.11	9.94 \pm 1.06
	TPM		0.19 \pm 0.12	8.75 \pm 2.44	2.06 \pm 2.01	9.47 \pm 1.06
	SIAM		0.61 \pm 0.17	9.67 \pm 4.50	0.71 \pm 0.14	9.84 \pm 3.30
	TDM		0.65 \pm 0.16	11.43 \pm 6.04	0.73 \pm 0.14	10.24 \pm 3.30
	TPDM		0.64 \pm 0.16	11.11 \pm 5.83	0.73 \pm 0.14	10.14 \pm 3.30
	PIA _{GSI}		0.82 \pm 1.96	7.57 \pm 4.30	0.94 \pm 0.06	6.75 \pm 1.03
	PIA ⁻		0.81 \pm 1.96	6.85 \pm 3.80	0.94 \pm 0.06	6.37 \pm 0.92
	PIA ⁺		0.81 \pm 1.96	6.26 \pm 3.66	0.94 \pm 0.06	6.13 \pm 0.74
<i>Betula pendula</i>	CDD	3,323	0.09 \pm 0.10	10.04 \pm 2.73	0.44 \pm 0.78	10.21 \pm 1.02
	DM1		0.15 \pm 0.11	9.54 \pm 2.64	2.31 \pm 2.58	9.54 \pm 1.05
	DM2		0.11 \pm 0.09	9.72 \pm 2.66	2.26 \pm 2.45	9.93 \pm 1.06
	TPM		0.19 \pm 0.12	9.33 \pm 2.64	2.10 \pm 2.10	9.47 \pm 1.05
	SIAM		0.58 \pm 0.19	11.27 \pm 5.69	0.72 \pm 0.16	9.85 \pm 3.36
	TDM		0.62 \pm 0.18	10.75 \pm 5.39	0.75 \pm 0.15	10.25 \pm 3.37
	TPDM		0.62 \pm 0.18	10.51 \pm 5.13	0.75 \pm 0.15	10.15 \pm 3.35
	PIA _{GSI}		0.77 \pm 0.14	7.71 \pm 4.13	0.95 \pm 0.08	6.71 \pm 1.05
	PIA ⁻		0.76 \pm 0.14	7.62 \pm 3.94	0.95 \pm 0.08	6.42 \pm 0.93
	PIA ⁺		0.77 \pm 0.14	6.96 \pm 3.69	0.95 \pm 0.08	6.19 \pm 0.74
<i>Fagus sylvatica</i>	CDD	3,037	0.11 \pm 0.12	9.41 \pm 2.74	0.56 \pm 0.71	10.24 \pm 1.04
	DM1		0.17 \pm 0.12	8.91 \pm 2.63	1.90 \pm 2.19	9.52 \pm 1.05
	DM2		0.14 \pm 0.11	9.13 \pm 2.62	1.89 \pm 1.98	9.92 \pm 1.06
	TPM		0.22 \pm 0.13	8.69 \pm 2.63	1.78 \pm 1.54	9.46 \pm 1.06
	SIAM		0.56 \pm 0.19	11.51 \pm 5.87	0.69 \pm 0.17	9.87 \pm 3.37
	TDM		0.60 \pm 0.19	11.16 \pm 5.55	0.73 \pm 0.16	10.27 \pm 3.37
	TPDM		0.60 \pm 0.19	11.06 \pm 5.38	0.73 \pm 0.16	10.17 \pm 3.37
	PIA _{GSI}		0.75 \pm 0.15	7.58 \pm 4.11	0.94 \pm 0.08	6.73 \pm 1.04

	PIA ⁻		0.74±0.15	7.59±4.22	0.94±0.08	6.38±0.93
	PIA ⁺		0.75±0.15	7.02±4.17	0.94±0.08	6.17±0.75
<i>Larix decidua</i>	CDD	1,070	0.13±0.13	8.44±3.29	0.40±0.67	10.23±1.00
	DM1		0.21±0.16	7.64±3.18	1.51±1.89	9.57±1.02
	DM2		0.18±0.14	7.82±3.22	1.66±1.68	9.93±1.06
	TPM		0.28±0.15	7.40±3.16	1.77±1.47	9.45±1.10
	SIAM		0.53±0.22	9.73±5.33	0.63±0.22	9.92±3.32
	TDM		0.57±0.22	11.65±6.51	0.67±0.21	10.32±3.32
	TPDM		0.57±0.21	11.52±6.41	0.67±0.21	10.22±3.32
	PIA _{GSI}		0.76±0.18	7.88±4.38	0.91±0.13	6.73±1.02
	PIA ⁻		0.75±0.18	5.97±3.64	0.91±0.13	6.38±0.94
	PIA ⁺		0.75±0.18	5.40±3.38	0.91±0.13	6.17±0.75
<i>Quercus robur</i>	CDD	2,834	0.10±0.11	9.65±2.68	0.54±0.69	10.21±1.01
	DM1		0.16±0.12	9.19±2.62	1.58±2.03	9.50±1.06
	DM2		0.11±0.10	9.43±2.62	1.70±1.83	9.92±1.05
	TPM		0.22±0.13	8.92±2.62	1.86±1.68	9.43±1.07
	SIAM		0.62±0.17	9.53±4.27	0.72±0.15	9.89±3.36
	TDM		0.66±0.17	10.16±4.51	0.75±0.14	10.28±3.36
	TPDM		0.66±0.16	10.28±4.48	0.75±0.14	10.18±3.36
	PIA _{GSI}		0.82±0.11	5.89±2.69	0.95±0.07	6.70±1.02
	PIA ⁻		0.82±0.11	5.92±2.74	0.95±0.07	6.38±0.93
	PIA ⁺		0.81±0.12	5.48±2.62	0.95±0.06	6.17±0.74
<i>Sorbus aucuparia</i>	CDD	936	0.12±0.13	9.50±3.23	0.47±0.69	10.21±1.00
	DM1		0.18±0.14	8.91±3.15	1.67±2.20	9.51±1.04
	DM2		0.14±0.12	9.16±3.17	1.76±2.00	9.96±1.05
	TPM		0.25±0.13	8.58±3.14	1.81±1.53	9.47±1.10
	SIAM		0.53±0.22	13.99±8.06	0.67±0.22	9.81±3.34
	TDM		0.59±0.21	11.81±7.03	0.73±0.20	10.21±3.34
	TPDM		0.59±0.22	11.64±6.82	0.73±0.20	6.74±1.04
	PIA _{GSI}		0.72±0.18	7.60±4.53	0.93±0.12	6.40±1.04
	PIA ⁻		0.70±0.19	7.70±4.39	0.92±0.13	6.40±0.95
	PIA ⁺		0.70±0.20	6.99±4.07	0.92±0.12	6.15±0.75

Table S5. Parameters and constants used in the model equations. Constant values for the photosynthesis model and water balance module refer to refs (27, 58), respectively.

Description	Abbreviation	Units	Value
Photosynthesis			
Total day-time net photosynthetic rate	$A_{\text{tot}}(\text{d})$	$\text{g C m}^{-2} \text{ day}^{-1}$	
Daily carbon assimilation (NPP)	$A_{\text{net}}(\text{d})$	$\text{g C m}^{-2} \text{ day}^{-1}$	
Daily gross photosynthesis (GPP)	$A_{\text{gross}}(\text{d})$	$\text{g C m}^{-2} \text{ day}^{-1}$	
Light limited rate	J_i	$\text{g C m}^{-2} \text{ day}^{-1}$	
Rubisco carboxylation limited rate	J_c	$\text{g C m}^{-2} \text{ day}^{-1}$	
Electron-transport limited rate	J_e	$\text{g C m}^{-2} \text{ day}^{-1}$	
Daily leaf respiration or CO ₂ release	$R(\text{d})$	$\text{g C m}^{-2} \text{ day}^{-1}$	
Maximum Rubisco capacity	V_{max}	$\text{g C m}^{-2} \text{ day}^{-1}$	
Daily integral of absorbed photosynthetically active radiation	APAR	$\text{J m}^{-2} \text{ day}^{-1}$	
Daylength	DL	hours day^{-1}	
Daily mean temperature	T	$^{\circ}\text{C day}^{-1}$	
Intercellular partial pressure of CO ₂	p_i	Pa	
Ambient partial pressure of O ₂	p_{O_2}	kPa	20.9
Atmospheric pressure	p	kPa	100.0
Fraction of PAR assimilated at ecosystem level relative to leaf level	α_a	–	0.5
Conversion factor for solar radiation from W m^{-2} to mol m^{-2}	C_q	–	2.04×10^{-6}
Co-limitation shape parameters by light and Rubisco activity	Θ	–	0.7
Leaf respiration as a fraction of Rubisco capacity in C ₃ plants	a	–	0.015
Intrinsic quantum efficiency of CO ₂ uptake in C ₃ plants	α	–	0.08
Optimal ratio of intercellular to ambient CO ₂ in C ₃ plants	λ	–	0.8
Atomic mass of carbon	C_{mass}	mol C m^{-2}	12.0
Michaelis constant at 25 degC (Q ₁₀ temperature dependency of CO ₂)	$k_{c,25}$	Pa	30.0
O ₂ inhibition constant at 25 degC	$k_{o,25}$	Pa	3000.0
CO ₂ /O ₂ specificity ratio	τ_{25}	–	2600

Water-balance

Water stress factor	$w(d)$	mm d^{-1}	
Atmospheric water demand	E_{demand}	mm d^{-1}	
Plant-controlled supply function	E_{supply}	mm d^{-1}	
Plant root-weighted soil moisture availability	$w_r(d)$	mm d^{-1}	
Daily potential evapotranspiration rate	$E_{\text{pot}}(d)$	mm d^{-1}	
Daily equilibrium evapotranspiration rate	$E_q(d)$	mm d^{-1}	
Non-water stressed canopy conductance	g_{pot}	mm s^{-1}	
Soil moisture at 0-10 cm and 10-40 cm	w_1 and w_2	mm d^{-1}	
Daily net solar radiation	R_n	$\text{W m}^{-2} \text{d}^{-1}$	
Daily downward short-wave radiation	R_s	$\text{W m}^{-2} \text{d}^{-1}$	
Daily upward long-wave radiation	R_l	$\text{W m}^{-2} \text{d}^{-1}$	
Daily soil temperature	T_{soil}	K day^{-1}	
Maximum transpiration rate	E_{max}	mm d^{-1}	5.0
Snow melt rate	k_{melt}	$\text{mm } ^\circ\text{C}^{-1} \text{d}^{-1}$	3.0
Maximum Priestley-Taylor coefficient	a_m	–	1.391
Scaling conductance	g_m	mm s^{-1}	3.26
PFT-dependent constant for minimum canopy conductance	g_{min}	mm s^{-1}	0.5 or 0.3
Psychrometer constant gamma	γ	Pa K^{-1}	65.0
Latent heat of vaporization of water	L	J kg^{-1}	2.5×10^6
Stefan-Boltzman constant	k_{sb}	$\text{W m}^{-2} \text{K}^{-4}$	5.67×10^{-8}
Emissivity for deciduous and coniferous plants	k_e	–	0.9

Table S6. Environmental conditions in experiment 2. The table depicts minimum and maximum daily temperatures set in the ambient and warmed chambers, average humidity, and day length. Day length in hours, humidity in %, temperature in °C. Note that the experiment started in June, and we shifted the monthly climate conditions by two months (e.g., the climate settings for July [actual month] reflected those typically occurring in May [climatic month]).

Actual month	Climatic month	Day length	Humidity	Ambient		Warming treatments	
				Min temp	Max temp	Min temp	Max temp
June	May	14.5	73	7.2	16.8	12.2	21.8
July	May	14.5	73	7.2	16.8	12.2	21.8
August	June	16.2	74	11.2	19.2	16.2	24.2
September	July	14.5	72	12.8	24.3	17.8	29.3
October	August	13	78	12.6	22.1	17.6	27.1
November	September	11.5	81	9.6	17.7	14.6	22.7

References and Notes

1. S. S. Renner, C. M. Zohner, Climate Change and Phenological Mismatch in Trophic Interactions Among Plants, Insects, and Vertebrates. *Annu. Rev. Ecol. Evol. Syst.* **49**, 165–182 (2018).
2. C. M. Zohner, S. S. Renner, Innately shorter vegetation periods in North American species explain native-non-native phenological asymmetries. *Nat. Ecol. Evol.* **1**, 1655–1660 (2017).
3. A. D. Richardson, T. F. Keenan, M. Migliavacca, Y. Ryu, O. Sonnentag, M. Toomey, Climate change, phenology, and phenological control of vegetation feedbacks to the climate system. *Agric. For. Meteorol.* **169**, 156–173 (2013).
4. A. Menzel, P. Fabian, Growing season extended in Europe. *Nature* **397**, 659 (1999).
5. T. F. Keenan, J. Gray, M. A. Friedl, M. Toomey, G. Bohrer, D. Y. Hollinger, J. W. Munger, J. O’Keefe, H. P. Schmid, I. S. Wing, B. Yang, A. D. Richardson, Net carbon uptake has increased through warming-induced changes in temperate forest phenology. *Nat. Clim. Chang.* **4**, 598–604 (2014).
6. A. D. Richardson, R. S. Anderson, M. A. Arain, A. G. Barr, G. Bohrer, G. Chen, J. M. Chen, P. Ciais, K. J. Davis, A. R. Desai, M. C. Dietze, D. Dragoni, S. R. Garrity, C. M. Gough, R. Grant, D. Y. Hollinger, H. A. Margolis, H. McCaughey, M. Migliavacca, R. K. Monson, J. W. Munger, B. Poulter, B. M. Raczka, D. M. Ricciuto, A. K. Sahoo, K. Schaefer, H. Tian, R. Vargas, H. Verbeeck, J. Xiao, Y. Xue, Terrestrial biosphere models need better representation of vegetation phenology: Results from the North American Carbon Program Site Synthesis. *Glob. Change Biol.* **18**, 566–584 (2012).
7. C. M. Zohner, L. Mo, T. A. M. Pugh, J. F. Bastin, T. W. Crowther, Interactive climate factors restrict future increases in spring productivity of temperate and boreal trees. *Glob. Change Biol.* **26**, 4042–4055 (2020).
8. M. Chen, E. K. Melaas, J. M. Gray, M. A. Friedl, A. D. Richardson, A new seasonal-deciduous spring phenology submodel in the Community Land Model 4.5: Impacts on carbon and water cycling under future climate scenarios. *Glob. Change Biol.* **22**, 3675–3688 (2016).
9. C. M. Zohner, L. Mo, S. S. Renner, J.-C. Svenning, Y. Vitasse, B. M. Benito, A. Ordonez, F. Baumgarten, J.-F. Bastin, V. Sebold, P. B. Reich, J. Liang, G.-J. Nabuurs, S. de-Miguel, G. Alberti, C. Antón-Fernández, R. Balazy, U.-B. Brändli, H. Y. H. Chen, C. Chisholm, E. Cenciala, S. Dayanandan, T. M. Fayle, L. Frizzera, D. Gianelle, A. M. Jagodzinski, B. Jaroszewicz, T. Jucker, S. Kepfer-Rojas, M. L. Khan, H. S. Kim, H. Korjus, V. K. Johannsen, D. Laarmann, M. Lang, T. Zawila-Niedzwiecki, P. A. Niklaus, A. Paquette, H. Pretzsch, P. Saikia, P. Schall, V. Šebeň, M. Svoboda, E. Tikhonova, H. Viana, C. Zhang, X. Zhao, T. W. Crowther, Late-spring frost risk between 1959 and 2017 decreased in North America but increased in Europe and Asia. *Proc. Natl. Acad. Sci. U.S.A.* **117**, 12192–12200 (2020).
10. A. S. Gallinat, R. B. Primack, D. L. Wagner, Autumn, the neglected season in climate change research. *Trends Ecol. Evol.* **30**, 169–176 (2015).

11. G. Liu, X. Chen, Y. Fu, N. Delpierre, Modelling leaf coloration dates over temperate China by considering effects of leafy season climate. *Ecol. Modell.* **394**, 34–43 (2019).
12. N. Delpierre, E. Dufrêne, K. Soudani, E. Ulrich, S. Cecchini, J. Boé, C. François, Modelling interannual and spatial variability of leaf senescence for three deciduous tree species in France. *Agric. For. Meteorol.* **149**, 938–948 (2009).
13. L. Chen, H. Hänninen, S. Rossi, N. G. Smith, S. Pau, Z. Liu, G. Feng, J. Gao, J. Liu, Leaf senescence exhibits stronger climatic responses during warm than during cold autumns. *Nat. Clim. Chang.* **10**, 777–780 (2020).
14. Y. S. H. Fu, M. Campioli, Y. Vitasse, H. J. De Boeck, J. Van den Berge, H. Abdelgawad, H. Asard, S. Piao, G. Deckmyn, I. A. Janssens, Variation in leaf flushing date influences autumnal senescence and next year's flushing date in two temperate tree species. *Proc. Natl. Acad. Sci. U.S.A.* **111**, 7355–7360 (2014).
15. T. F. Keenan, A. D. Richardson, The timing of autumn senescence is affected by the timing of spring phenology: Implications for predictive models. *Glob. Change Biol.* **21**, 2634–2641 (2015).
16. C. M. Zohner, S. S. Renner, Ongoing seasonally uneven climate warming leads to earlier autumn growth cessation in deciduous trees. *Oecologia* **189**, 549–561 (2019).
17. M. J. Paul, C. H. Foyer, Sink regulation of photosynthesis. *J. Exp. Bot.* **52**, 1383–1400 (2001).
18. A. Miller, C. Schlagnhauser, M. Spalding, S. Rodermel, Carbohydrate regulation of leaf development: Prolongation of leaf senescence in Rubisco antisense mutants of tobacco. *Photosynth. Res.* **63**, 1–8 (2000).
19. Y. H. Fu, S. Piao, N. Delpierre, F. Hao, H. Hänninen, X. Geng, J. Peñuelas, X. Zhang, I. A. Janssens, M. Campioli, Nutrient availability alters the correlation between spring leaf-out and autumn leaf senescence dates. *Tree Physiol.* **39**, 1277–1284 (2019).
20. M. R. Guitman, P. A. Arnozis, A. J. Barneix, Effect of source-sink relations and nitrogen nutrition on senescence and N remobilization in the flag leaf of wheat. *Physiol. Plant.* **82**, 278–284 (1991).
21. R. Kumar, E. Bishop, W. C. Bridges, N. Tharayil, R. S. Sekhon, Sugar partitioning and source-sink interaction are key determinants of leaf senescence in maize. *Plant Cell Environ.* **42**, 2597–2611 (2019).
22. P. B. Reich, M. B. Walters, D. S. Ellsworth, Leaf life-span in relation to leaf, plant, and stand characteristics among diverse ecosystems. *Ecol. Monogr.* **62**, 365–392 (1992).
23. W. Buermann, M. Forkel, M. O'Sullivan, S. Sitch, P. Friedlingstein, V. Haverd, A. K. Jain, E. Kato, M. Kautz, S. Lienert, D. Lombardozzi, J. E. M. S. Nabel, H. Tian, A. J. Wiltshire, D. Zhu, W. K. Smith, A. D. Richardson, Widespread seasonal compensation effects of spring warming on northern plant productivity. *Nature* **562**, 110–114 (2018).
24. J. U. Jepsen, L. Kapari, S. B. Hagen, T. Schott, O. P. L. Vindstad, A. C. Nilssen, R. A. Ims, Rapid northwards expansion of a forest insect pest attributed to spring phenology matching with sub-Arctic birch. *Glob. Change Biol.* **17**, 2071–2083 (2011).

25. B. Templ, E. Koch, K. Bolmgren, M. Ungersböck, A. Paul, H. Scheifinger, T. Rutishauser, M. Busto, F.-M. Chmielewski, L. Hájková, S. Hodzić, F. Kaspar, B. Pietragalla, R. Romero-Fresneda, A. Tolvanen, V. Vučetić, K. Zimmermann, A. Zust, Pan European Phenological database (PEP725): A single point of access for European data. *Int. J. Biometeorol.* **62**, 1109–1113 (2018).
26. Materials and methods are available as supplementary materials.
27. S. Sitch, B. Smith, I. C. Prentice, A. Arneth, A. Bondeau, W. Cramer, J. O. Kaplan, S. Levis, W. Lucht, M. T. Sykes, K. Thonicke, S. Venevsky, Evaluation of ecosystem dynamics, plant geography and terrestrial carbon cycling in the LPJ dynamic global vegetation model. *Glob. Change Biol.* **9**, 161–185 (2003).
28. W. M. Jolly, R. Nemani, S. W. Running, A generalized, bioclimatic index to predict foliar phenology in response to climate. *Glob. Change Biol.* **11**, 619–632 (2005).
29. M. Meinshausen, E. Vogel, A. Nauels, K. Lorbacher, N. Meinshausen, D. M. Etheridge, P. J. Fraser, S. A. Montzka, P. J. Rayner, C. M. Trudinger, P. B. Krummel, U. Beyerle, J. G. Canadell, J. S. Daniel, I. G. Enting, R. M. Law, C. R. Lunder, S. O'Doherty, R. G. Prinn, S. Reimann, M. Rubino, G. J. M. Velders, M. K. Vollmer, R. H. J. Wang, R. Weiss, Historical greenhouse gas concentrations for climate modelling (CMIP6). *Geosci. Model Dev.* **10**, 2057–2116 (2017).
30. Y. Xie, X. Wang, A. M. Wilson, J. A. Silander Jr., Predicting autumn phenology: How deciduous tree species respond to weather stressors. *Agric. For. Meteorol.* **250–251**, 127–137 (2018).
31. G. Liu, X. Chen, Q. Zhang, W. Lang, N. Delpierre, Antagonistic effects of growing season and autumn temperatures on the timing of leaf coloration in winter deciduous trees. *Glob. Change Biol.* **24**, 3537–3545 (2018).
32. B. Smith, D. Wårlind, A. Arneth, T. Hickler, P. Leadley, J. Siltberg, S. Zaehle, Implications of incorporating N cycling and N limitations on primary production in an individual-based dynamic vegetation model. *Biogeosciences* **11**, 2027–2054 (2014).
33. M. T. Sykes, I. C. Prentice, W. Cramer, A bioclimatic model for the potential distributions of North European tree species under present and future climates. *J. Biogeogr.* **23**, 203–233 (1996).
34. J. Mao, A. Ribes, B. Yan, X. Shi, P. E. Thornton, R. Séférian, P. Ciais, R. B. Myneni, H. Douville, S. Piao, Z. Zhu, R. E. Dickinson, Y. Dai, D. M. Ricciuto, M. Jin, F. M. Hoffman, B. Wang, M. Huang, X. Lian, Human-induced greening of the northern extratropical land surface. *Nat. Clim. Chang.* **6**, 959–963 (2016).
35. A. Fangmeier, B. Chrost, P. Högy, K. Krupinska, CO₂ enrichment enhances flag leaf senescence in barley due to greater grain nitrogen sink capacity. *Environ. Exp. Bot.* **44**, 151–164 (2000).
36. S. C. Wong, Elevated atmospheric partial pressure of CO₂ and plant growth : II. Non-structural carbohydrate content in cotton plants and its effect on growth parameters. *Photosynth. Res.* **23**, 171–180 (1990).

37. C. Körner, Towards a better experimental basis for upscaling plant responses to elevated CO₂ and climate warming. *Plant Cell Environ.* **18**, 1101–1110 (1995).
38. C. M. Zohner, A. Rockinger, S. S. Renner, Increased autumn productivity permits temperate trees to compensate for spring frost damage. *New Phytol.* **221**, 789–795 (2019).
39. A. P. Walker, M. G. De Kauwe, A. Bastos, S. Belmecheri, K. Georgiou, R. F. Keeling, S. M. McMahon, B. E. Medlyn, D. J. P. Moore, R. J. Norby, S. Zaehle, K. J. Anderson-Teixeira, G. Battipaglia, R. J. W. Brienen, K. G. Cabugao, M. Cailleret, E. Campbell, J. G. Canadell, P. Ciais, M. E. Craig, D. S. Ellsworth, G. D. Farquhar, S. Fatichi, J. B. Fisher, D. C. Frank, H. Graven, L. Gu, V. Haverd, K. Heilman, M. Heimann, B. A. Hungate, C. M. Iversen, F. Joos, M. Jiang, T. F. Keenan, J. Knauer, C. Körner, V. O. Leshyk, S. Leuzinger, Y. Liu, N. MacBean, Y. Malhi, T. R. McVicar, J. Penuelas, J. Pongratz, A. S. Powell, T. Riutta, M. E. B. Sabot, J. Schleucher, S. Sitch, W. K. Smith, B. Sulman, B. Taylor, C. Terrer, M. S. Torn, K. K. Treseder, A. T. Trugman, S. E. Trumbore, P. J. van Mantgem, S. L. Voelker, M. E. Whelan, P. A. Zuidema, Integrating the evidence for a terrestrial carbon sink caused by increasing atmospheric CO₂. *New Phytol.* **nph.16866** (2020).
40. P. O. Lim, H. J. Kim, H. G. Nam, Leaf senescence. *Annu. Rev. Plant Biol.* **58**, 115–136 (2007).
41. N. Sade, M. Del Mar Rubio-Wilhelmi, K. Umnajkitikorn, E. Blumwald, Stress-induced senescence and plant tolerance to abiotic stress. *J. Exp. Bot.* **69**, 845–853 (2018).
42. H. R. Woo, H. J. Kim, P. O. Lim, H. G. Nam, Leaf Senescence: Systems and Dynamics Aspects. *Annu. Rev. Plant Biol.* **70**, 347–376 (2019).
43. B. D. Hesse, M. Goisser, H. Hartmann, T. E. E. Grams, Repeated summer drought delays sugar export from the leaf and impairs phloem transport in mature beech. *Tree Physiol.* **39**, 192–200 (2019).
44. C. Terrer, R. B. Jackson, I. C. Prentice, T. F. Keenan, C. Kaiser, S. Vicca, J. B. Fisher, P. B. Reich, B. D. Stocker, B. A. Hungate, J. Peñuelas, I. McCallum, N. A. Soudzilovskaia, L. A. Cernusak, A. F. Talhelm, K. Van Sundert, S. Piao, P. C. D. Newton, M. J. Hovenden, D. M. Blumenthal, Y. Y. Liu, C. Müller, K. Winter, C. B. Field, W. Viechtbauer, C. J. Van Lissa, M. R. Hoosbeek, M. Watanabe, T. Koike, V. O. Leshyk, H. W. Polley, O. Franklin, Nitrogen and phosphorus constrain the CO₂ fertilization of global plant biomass. *Nat. Clim. Chang.* **9**, 684–689 (2019).
45. G. Taylor, M. J. Tallis, C. P. Giardina, K. Percy, F. Miglietta, P. S. Gupta, B. Gioli, C. Calfapietra, B. Gielen, M. Kubiske, G. Scarascia-Mugnozza, K. Kets, S. P. Long, D. F. Karnosky, Future atmospheric CO₂ leads to delayed autumnal senescence. *Glob. Change Biol.* **14**, 264–275 (2008).
46. [zanid90/AutumnPhenology](#): Autumn Phenology repository, Zenodo (2020); .
47. Y. Vitasse, C. Signarbieux, Y. H. Fu, Global warming leads to more uniform spring phenology across elevations. *Proc. Natl. Acad. Sci. U.S.A.* **115**, 1004–1008 (2018).
48. M. Rodell, P. R. Houser, U. Jambor, J. Gottschalck, K. Mitchell, C.-J. Meng, K. Arsenault, B. Cosgrove, J. Radakovich, M. Bosilovich, J. K. Entin, J. P. Walker, D. Lohmann, D.

- Toll, The Global Land Data Assimilation System. *Bull. Am. Meteorol. Soc.* **85**, 381–394 (2004).
49. C. Beer, U. Weber, E. Tomelleri, N. Carvalhais, M. Mahecha, M. Reichstein, Harmonized European Long-Term Climate Data for Assessing the Effect of Changing Temporal Variability on Land–Atmosphere CO₂ Fluxes*. *J. Clim.* **27**, 4815–4834 (2014).
 50. T. Hengl, J. Mendes de Jesus, G. B. M. Heuvelink, M. Ruiperez Gonzalez, M. Kilibarda, A. Blagotić, W. Shangguan, M. N. Wright, X. Geng, B. Bauer-Marschallinger, M. A. Guevara, R. Vargas, R. A. MacMillan, N. H. Batjes, J. G. B. Leenaars, E. Ribeiro, I. Wheeler, S. Mantel, B. Kempen, SoilGrids250m: Global gridded soil information based on machine learning. *PLOS ONE* **12**, e0169748 (2017).
 51. J. Moeys, soiltexture: Functions for Soil Texture Plot, Classification and Transformation (2018); <https://cran.r-project.org/package=soiltexture>.
 52. B. D. Stocker, H. Wang, N. G. Smith, S. P. Harrison, T. F. Keenan, D. Sandoval, T. Davis, I. C. Prentice, P-model v1.0: An optimality-based light use efficiency model for simulating ecosystem gross primary production. *Geosci. Model Dev.* **13**, 1545–1581 (2020).
 53. H. Wang, I. C. Prentice, T. F. Keenan, T. W. Davis, I. J. Wright, W. K. Cornwell, B. J. Evans, C. Peng, Towards a universal model for carbon dioxide uptake by plants. *Nat. Plants* **3**, 734–741 (2017).
 54. I. C. Prentice, N. Dong, S. M. Gleason, V. Maire, I. J. Wright, Balancing the costs of carbon gain and water transport: Testing a new theoretical framework for plant functional ecology. *Ecol. Lett.* **17**, 82–91 (2014).
 55. S. Running, Q. Mu, M. Zhao, MOD17A3 MODros. Inf. Serv./Terra Net Primary Production Yearly L4 Global 1 km SIN Grid V055, NASA EOSDIS Land Processes DAAC (2011); (2011); <https://lpdaac.usgs.gov/products/mod17a3hgfv006>.
 56. MODros. Inf. Serv./Terra+Aqua Land Cover Type Yearly L3 Global 500 m SIN Grid. MCD12Q1 v006 (2019); <https://doi.org/10.5067/MODIS/MCD12Q1.006>.
 57. M. C. Hansen, P. V. Potapov, R. Moore, M. Hancher, S. A. Turubanova, A. Tyukavina, D. Thau, S. V. Stehman, S. J. Goetz, T. R. Loveland, A. Kommareddy, A. Egorov, L. Chini, C. O. Justice, J. R. G. Townshend, High-resolution global maps of 21st-century forest cover change. *Science* **342**, 850–853 (2013).
 58. D. Gerten, S. Schaphoff, U. Haberlandt, W. Lucht, S. Sitch, Terrestrial vegetation and water balance—Hydrological evaluation of a dynamic global vegetation model. *J. Hydrol. (Amst.)* **286**, 249–270 (2004).
 59. M. Huang, S. Piao, P. Ciais, J. Peñuelas, X. Wang, T. F. Keenan, S. Peng, J. A. Berry, K. Wang, J. Mao, R. Alkama, A. Cescatti, M. Cuntz, H. De Deurwaerder, M. Gao, Y. He, Y. Liu, Y. Luo, R. B. Myneni, S. Niu, X. Shi, W. Yuan, H. Verbeeck, T. Wang, J. Wu, I. A. Janssens, Air temperature optima of vegetation productivity across global biomes. *Nat. Ecol. Evol.* **3**, 772–779 (2019).
 60. A. Haxeltine, I. C. Prentice, BIOME3: An equilibrium terrestrial biosphere model based on ecophysiological constraints, resource availability, and competition among plant functional types. *Global Biogeochem. Cycles* **10**, 693–709 (1996).

61. C. Huntingford, J. L. Monteith, The behaviour of a mixed-layer model of the convective boundary layer coupled to a big leaf model of surface energy partitioning. *Boundary-Layer Meteorol.* **88**, 87–101 (1998).
62. W. L. Bauerle, R. Oren, D. A. Way, S. S. Qian, P. C. Stoy, P. E. Thornton, J. D. Bowden, F. M. Hoffman, R. F. Reynolds, Photoperiodic regulation of the seasonal pattern of photosynthetic capacity and the implications for carbon cycling. *Proc. Natl. Acad. Sci. U.S.A.* **109**, 8612–8617 (2012).
63. S. Kim, ppcor: Partial and Semi-Partial (Part) Correlation (R package version 1.1, 2015); <https://cran.r-project.org/package=ppcor>.
64. J. S. Lefcheck, piecewiseSEM: Piecewise structural equation modelling in r for ecology, evolution, and systematics. *Methods Ecol. Evol.* **7**, 573–579 (2016).
65. E. Dufrêne, H. Davi, C. François, G. le Maire, V. Le Dantec, A. Granier, Modelling carbon and water cycles in a beech forest: Part I: Model description and uncertainty analysis on modelled NEE. *Ecol. Modell.* **185**, 407–436 (2005).
66. W. Lang, X. Chen, S. Qian, G. Liu, S. Piao, A new process-based model for predicting autumn phenology: How is leaf senescence controlled by photoperiod and temperature coupling? *Agric. For. Meteorol.* **268**, 124–135 (2019).
67. K. Hufkens, D. Basler, T. Milliman, E. K. Melaas, A. D. Richardson, An integrated phenology modelling framework in r. *Methods Ecol. Evol.* **9**, 1276–1285 (2018).
68. C. Tsallis, D. A. Stariolo, Generalized simulated annealing. *Physica A* **233**, 395–406 (1996).
69. D. Basler, Evaluating phenological models for the prediction of leaf-out dates in six temperate tree species across central Europe. *Agric. For. Meteorol.* **217**, 10–21 (2016).
70. M. G. R. Cannell, R. I. Smith, Thermal time, chill days and prediction of bud burst in *Picea sitchensis*. *J. Appl. Ecol.* **20**, 951–963 (1983).
71. K. Blümel, F. M. Chmielewski, Shortcomings of classical phenological forcing models and a way to overcome them. *Agric. For. Meteorol.* **164**, 10–19 (2020).
72. H. Hänninen, Modelling bud dormancy release in trees from cool and temperate regions. *Acta Forestalia Fennica* **213**, 1–47 (1990).